Decomposing kinetic energy along Line P in the Pacific ocean

by

Manman Wang
B.Sc., Ocean University of China, 2012

A Thesis Submitted in Partial Fulfillment of the
Requirements for the Degree of

Master of Science

in the School of Earth and Ocean Science

Decomposing kinetic energy along Line P in the Pacific ocean

by

Manman Wang
B.Sc., Ocean University of China, 2012

Supervisory Committee

Dr. Jody Klymak, Supervisor
(School of Earth and Ocean Science)

Dr. Ann Gargett, Departmental Member
(School of Earth and Ocean Science)

Dr. Tetjana Ross, Outside Member
(Institute of Ocean Sciences, Dalhousie University)

Supervisory Committee

Dr. Jody Klymak, Supervisor
(School of Earth and Ocean Science)

Dr. Ann Gargett, Departmental Member
(School of Earth and Ocean Science)

Dr. Tetjana Ross, Outside Member
(Institute of Ocean Sciences, Dalhousie University)

ABSTRACT

The upper ocean is host to overlapping vortical and internal waves dynamics over the submesoscales (10-100km), both of which are poorly represented in eddy-resolving ocean models. We analyze upper-ocean (0-200 m) horizontal-wavenumber spectra along Line P in the North Pacific subpolar gyre from shipboard ADCP measurements in February and June (2013-2015), and compare them to spectra from a 1/36th degree numerical simulation output. At scales between 10 and 100 km, the ADCP along-track ($\hat{C}^u$) and across-track ($\hat{C}^v$) kinetic energy spectra approximately follow power laws of k^{-2} and have a ratio $R = \hat{C}^v/\hat{C}^u \simeq 1$. For purely non-divergent motions, the order of the power law and R should be the same, so divergent motions are evident. A Helmholtz decomposition estimates the fraction total kinetic energy that is contributed by internal-wave and vortex components. Vortex components follow a power law of k^{-2} with ratio $R \simeq 2$, consistent with predictions for a non-divergent flow, while internal waves are mostly consistent with the Garrett and Munk internal wave model. There are modest seasonal changes; vortical motions are slightly stronger in February than in June, whereas the amplitudes of the internal wave component increases in June. Depth variability of non-divergent vortical flows shows that at low wave-numbers energy decreases and that the kinetic energy spectra are bluer with depth, inconsistent with predictions from surface quasi-geostrophic theory of

redder spectra with depth. Conversely, in the simulation the depth variability of the decomposed vortex components is in agreement with predictions of surface quasi-geostrophic theory. The simulations had very weak internal waves fields.

Contents

List of Tables

List of Figures

ACKNOWLEDGEMENTS

I would like to thank:

my supervisor, Dr. Jody Klymak, for continuously encouraging me to overcome a lot of difficulties, and for infinite patience in guiding me through the details, especially with my writing.

my committee members, Dr. Ann Gargett and Dr. Tetjana Ross, for providing me valuable feedback on my work.

my office-mate Ken, for introducing me a lot of skills to be a good master student.

my family, husbund, friends, for all their support and inspiration.

A special thank you to Marie Robert who manages the Line P sampling program at the Institution of Ocean Sciences and other Line P participants who helped with data collection. This work could not have been possible without their contribution.

Chapter 1

Introduction

How ocean forcing at large scales cascades to turbulence has been investigated by oceanographers for a long time. The internal wave cascade is believed to be from large to small scales, and has received the most attention. The fate of mesoscale motions such as eddying by baroclinic instability is more poorly understood. Under the quasi-geostrophic assumption, two-dimensional turbulence will cascade energy from small to large scales in an inverse cascade. However, stirring by mesoscale motions can also intensify small-scale fronts, driving what is being called "submesoscale" variability in the range 10-100 km. Understanding of this direct cascade to smaller scales is hampered by a lack of observations at these scales, and by the superposition of internal wave motions at the same scales, often obscuring the "vortical" motions.

Submesoscale flows have been shown to have an impact on larger-scale flows and tracer distributions. Simulation studies suggest that enhanced vertical velocity induced by submesoscale motions can modify the physical properties of water subducted to the thermocline (Le Traon et al., 2008) as well as impact the biogeochemistry of the upper ocean (e.g. Mahadevan, 2014). Besides their effect on exchanges between the surface and interior ocean, energetic near-surface submesoscale flows have also been suggested to strongly affect the stratification of the upper ocean. However, our understanding of how deep the influence of surface-enhanced submesoscale flows can reach, and the vertical structure of submesoscale flows are not well known.

Another motivation for studying the submesoscale is closing the energy budget of the mesoscale. Mesoscale eddies are energized by thermocline baroclinic and barotropic instabilities and transfer energy to large scales. A proposed solution to how energy cascades from the mesoscale is that surface frontogenesis and ageostrophic submesoscale instabilities tend to overcome the constraints of stratification and ro-

tation, and transfer mesoscale energy to small dissipation scales (Molemaker et al., 2005, 2010, Capet et al., 2008a). Lapeyre and Klein (2006) suggested that surface quasi-geostrophic (QG) turbulence may be the relevant framework for interpreting the submesoscale turbulence that develops in response to frontogenesis.

The goal here is to analyze lateral slices of ocean currents along Line P in the subarctic Pacific collected from repeat Acoustic Doppler Current Profile (ADCP) measurements, and as simulated in a 1/36th of degree regional model. Spectra of kinetic energy are compared to expected spectral characteristics from the existing theories. Interior QG theory posits that flows are due to interior potential vorticity (PV) anomalies that are far from boundaries, and predict that kinetic energy follow a power law of k^{-3}. Surface QG theory assumes that the sources of vorticity are largest at the ocean surface, and predicts that the kinetic energy spectra follow a power law of $k^{-5/3}$ in the near-surface layer, and become more red at depth, such that far from the surface the follow a power law of k^{-3}. For both theories, the flow should be horizontally non-divergent of leading order, and therefore the ratio of across-track to the along-track spectra should be the same as the power law exponent.

There are few examples of lateral kinetic energy spectra in the ocean, suitable for teasing apart internal waves and vortical motions. Part of this has been because only recently have plausible methods for separating the two types of motion been proposed (Callies and Ferrari, 2013, Bühler et al., 2014). Wang et al. (2010) examined 10 years of the Oleander data set through the Gulf Stream in the surface mixed layer to avoid internal waves, and found steep kinetic energy spectra (k^{-3}), consistent with interior QG predictions. Callies and Ferrari (2013), Bühler et al. (2014) revisited this data below the mixed layer, and decomposed the internal waves and vortical motions, again finding k^{-3} in the vortical motions, added to relatively weak internal wave component. A similarly steep vortical spectrum was found when examining 13 years of ADCP transects across Drake Passage in the Southern Ocean (Rocha et al., 2016). On the other hand, a dataset from the subtropical North Pacific, far from any strong baroclinic boundary currents, yielded weaker vortical components to the flow, and much less steep spectral slopes of k^{-2} (Callies and Ferrari, 2013, Bühler et al., 2014). Unlike in the strong currents, the kinetic energy spectra were dominated by internal waves at scales smaller than 100 km.

In this thesis, a similar methodology to that used in Bühler et al. (2014), Rocha et al. (2016) is used to diagnose the dominant motions along Line P in the North Pacific by comparing observed kinetic energy spectra with existing theories. Line P

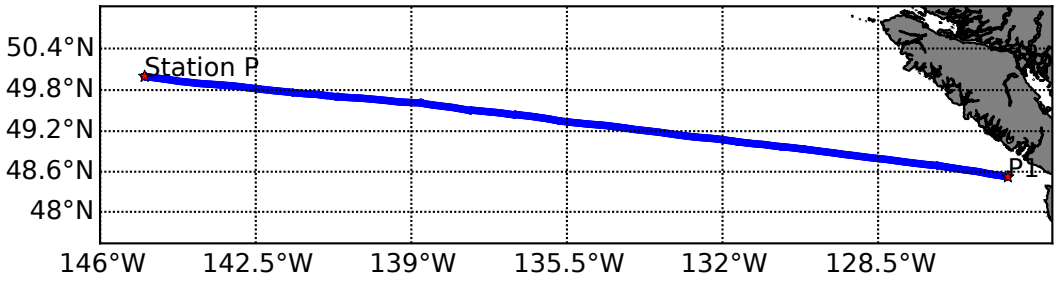

Figure 1.1: Maps showing Line Papa. Blue line on the map shows Line P transect, with two red stars show station P1 and Station P.

runs from the Strait of Juan de Fuca to Station P at 50 N, 145 W in the North Pacific (Fig. 1.1) (Crawford et al., 2007). The region experiences a strong seasonal change, producing mixed layers deeper than 100 m in winter time (Klymak et al., 2015). The surface water warms and restratifies in summer time. Seven available transects of ADCP measurements in February (four transects) and June (three transects) during 2013 - 2015 are used to examine if there are seasonal changes in the spectra. The goal here is to use available observations from the upper ocean in the North Pacific to diagnose if the flows in the submesoscale are geostrophically balanced or unbalanced motions. If the flow is balanced, can existing theories of geostrophic turbulence successfully describe the balanced part of the flow?

To answer these questions, following Bühler et al. (2014), the Helmholtz decomposition is applied (Chapter 3) to the kinetic energy spectra in order to decompose the energy into vortical balanced and wave-like unbalanced components. In addition, two main diagnostics are employed: spectral slopes and the ratio of across-track to along-track kinetic energy spectra. If the vortical flow is two-dimensional non-divergent flow, the ratio R would equal the absolute value of the slope. These diagnostics are applied to in situ velocity measurements and data from NEMO3.1 simulation (Chapter 4).

The upper-ocean kinetic energy spectra in the North Pacific are found to be dominated by a balanced non-divergent flow at scales between 40 km and 100 km and have power laws of k^{-2}. Evidence of depth independence are inconsistent with depth trend predicted by surface QG. Internal waves also make contributions over scales up to 100 km. Moreover, modest seasonal changes are observed; vortical motions are slightly stronger in February than in June, whereas the amplitude of the internal wave component increases in June. The inconsistency with surface QG of the kinetic

energy spectra agrees with spice spectra along Line P (Klymak et al., 2015).

The NEMO simulation of Line P exhibits steeper kinetic energy spectra with $k^{-2.5}$, almost all of which can be ascribed to balanced vortical motions; internal waves appear to be weak in the simulations.

The rest of this thesis is organized as follows:

Chapter 2 provides an review of existing theoretical predictions for the geostrophic turbulence flow and internal waves.

Chapter 3 reviews the method, Helmholtz decomposition, that is used to decompose the energy into wave and vortex components.

Chapter 4 describes data analysis for ADCP and model data with some results presented.

Chapter 5 discusses and compares energy spectra with theoretical predictions.

Chapter 6 concludes and makes suggestions of possible future work.

Chapter 2

Theory

This paper uses kinetic energy spectra to compare observations and simulation results to predictions from theories of quasi-geostrophic turbulence and the canonical Garret and Munk internal wave model. In order to compare with the theories, the spectral slopes are diagnosed, the ratio of across- and along-track spectral energy, and the change of amplitude and spectral slope with depth.

2.1 Theoretical predictions for submesoscale wavenumber spectra

Theories are normally expressed in terms of spectral power laws that can be used to diagnose different types of physical processes. Two variants of geostrophic-turbulent theory for submesoscale turbulence have been proposed: interior quasi-geostrophic (QG) turbulence, resulting from deep baroclinic instabilities (Charney, 1971); and surface QG turbulence (Blu), developing from surface frontogenesis. These drive largely lateral stirring motions (e.g. Stammer, 1997, Wang et al., 2010, Le Traon et al., 2008). At the same time, the internal-wave continuum may contribute significantly to submesoscale variability.

2.1.1 Quasi-geostrophic turbulence

Any QG flow can be decomposed into a component due to interior PV anomalies and a component resulting from surface frontogenesis (e.g. Lapeyre and Klein, 2006). Charney (1971) considered a flow due to interior PV anomalies that are far enough

from the surface boundaries that the effect of the surface buoyancy anomalies can be ignored. Under the assumptions of isotropy and homogeneity, interior QG predicts surface kinetic and potential energy spectra scale like k_h^{-3}, where k_h represents the isotropic horizontal wavenumber (Charney, 1971, Callies and Ferrari, 2013). Interior QG turbulence scalings, however, do not apply at and below the ocean surface.

As a complement, Blumen (1978) considered another type of flow associated with the surface frontogenesis, which is known as surface QG turbulence. In an ocean with constant stratification, spectra of surface kinetic and potential energy follow $k_h^{-5/3}$. Furthermore, assuming no interior sources of potential energy input, surface QG motions of horizontal scale $2\pi/k_h$ have a vertical decay scale f/Nk_h associated with inertial frequency f and buoyancy frequency N, which means high-wavenumber motions decay faster than low. At a given depth z_{decay}, modes with horizontal scale smaller than $-Nz_{decay}/f$ have decayed significantly while large-scale modes are essentially unattenuated. Simply, surface QG predicts spectra of kinetic- and potential energy that follow $k^{-5/3}$ above this transition scale and rapidly decay below (e.g. Callies and Ferrari, 2013, Scott, 2006). Note that predictions of surface QG assumes only weak ageostrophic motions.

In an ocean with constant stratification, under the same assumption, surface QG predicts that spectra of kinetic and potential energy spectra follow $k_h^{-5/3}$ (Blu) (Fig. 2.1a). In an ocean with non-constant stratification potential energy spectra still follow $k_h^{-5/3}$, but kinetic energy spectra differ roll off at wavelengths larger than the internal radius of deformation (LaCasce, 2012) (Fig. 2.1b). Surface mixed layers modify the lower wavenumbers further (Callies and Ferrari, 2013).

The power laws predicted by surface QG theory, however, need to be revised to account for contributions of ageostrophic flows (Capet et al., 2008b). It has been shown that the flattening of kinetic energy over low wave numbers compared with the slopes in interior QG turbulence are indicative of the creation of strong horizontal shears and sharp buoyancy gradients, the prelude of frontogenesis (e.g. Hoskins and Bretherton, 1972). If the advection by ageostrophic flow is added in Blumen's idealized flow (without considering the interior PV variation), the power law becomes k_h^{-2} at the surface (Boyd, 1992).

2.1.2 Internal waves

Ageostrophic motions (e.g. inertia-gravity waves, mixed layer instabilities, tides, etc) also make a contribution to the submesoscale, which can flatten the spectra because they project onto small scale. Garrett and Munk (1972) spectrum is an empirical model (referred to as GM), which describes the internal wave field as separable vertical and temporal spectral shapes and amplitudes that are remarkably uniform across the ocean. We can derive lateral spectra using the linear consistency relations. These wavenumber spectra scale as $K(k_h) \sim P(k_h) \sim k_h^{-2}$ over high wavenumbers and flatten out at scales larger than about 10 km.

2.2 Relating two-dimensional spectral theories to the one-dimensional spectral observations

The predictions in the last section are described for two-dimensional isotropic spectra. Observations, however, are typically taken along a one-dimensional track and only one-dimensional spectra can be calculated as functions of along-track wavenumber k. The conversion between two-dimensional isotropic spectrum $S(k_h)$ to a one-dimensional spectrum $S(k)$ is given by (Batchelor, 1953)

$$S(k) = \frac{2}{\pi} \int_k^\infty \frac{S(k_h)}{({k_h}^2 - k^2)^{1/2}} dk_h \tag{2.1}$$

If the two-dimensional spectrum follows a power law $S(k_h) \sim k_h^{-n}$, $n > 0$, then the one-dimensional spectrum can be easily obtained, giving the same power law $S(k) \sim k^{-n}$. Thus the predicted scalings in Section 2.1 for the two-dimensional flow thus directly translate to the one-dimensional spectra of kinetic energy.

The one-dimensional spectra of the along- and across-track kinetic energy, $\hat{C}^u = \frac{1}{2}\langle u^2 \rangle$ and $\hat{C}^v = \frac{1}{2}\langle v^2 \rangle$ are not necessarily the same (u and v are the along- and across-track velocity components, respectively). Considering a two-dimensional flow (horizontally non-divergent), $\hat{C}^u(k)$ and $\hat{C}^v(k)$ relate to the two-dimensional isotropic spectrum $\hat{C}(k_h)$ by

$$non-divergent\ flow\ only: \hat{C}^u(k) = \frac{2}{\pi}\int_k^\infty \frac{\sqrt{k_h^2-k^2}}{k_h^2}\hat{C}(k_h)dk_h,$$
$$\hat{C}^v(k) = \frac{2}{\pi}k^2\int_k^\infty \frac{1}{k_h^2\sqrt{k_h^2-k^2}}\hat{C}(k_h)dk_h \tag{2.2}$$

By inspection,

$$\hat{C}^v(k) = -k\frac{d}{dk}\hat{C}^u(k). \tag{2.3}$$

is obtained.

Thus, if $\hat{C}^u(k)$ of an isotropic two-dimensional non-divergent flow has a power law of k_h^{-n}, then the relation between $\hat{C}^u(k)$ and $\hat{C}^v(k)$ can be established through the exponent in power law, which was observed by Charney when comparing his predictions for geostrophic turbulence against data (e.g. Batchelor, 1953, Charney, 1971, Leith, 1971)

$$\hat{C}^v(k) = n\hat{C}^u(k). \tag{2.4}$$

Relation 2.4 is particularly relevant for geostrophic turbulence, which is horizontally non-divergent at leading order and this relation will be used below. In addition, QG buoyancy is related to the vertical gradient of stream function and therefore the one-dimensional potential energy is related to the one-dimensional kinetic energy spectrum. For interior QG turbulence, the potential energy spectrum equals the along-track component of kinetic energy spectrum, $P(k) = \hat{C}^u(k)$ (Charney, 1971), while for surface QG turbulence it equals the total kinetic energy spectrum, $P(k) = \hat{C}^u(k) + \hat{C^v}(k)$ in the case of constant stratification. For a more realistic ocean, surface QG predicts that the kinetic energy spectrum to be lower than poten-

Table 2.1: Properties of one-dimensional wavenumber spectra ($\hat{C}^u(k)$ and $\hat{C}^v(k)$ are the along- and across-track kinetic energy spectra, $P(k)$ is the potential energy spectrum)

	QG turbulence			Internal-wave continuum
	Interior	Surface (constant N)	Surface (Non constant N)	
$\hat{C}^v(k)$ slopes	-3	-5/3 (at surface, steep below)	see Fig. 2.1	-2 (in small-scale roll-off)
Relation between $\hat{C}^u(k)$ and $\hat{C}^v(k)$	$\hat{C}^v(k) = 3\hat{C}^u(k)$	$\hat{C}^v(k) = 5/3\hat{C}^u(k)$(at surface)	see Fig. 2.1	$\hat{C}^u(k) = \hat{C}^v(k)$
Relation between $\hat{C}^u(k)$ and $\hat{C}^v(k)$ and $P(k)$	$P(k) = \hat{C}^v(k)$	$P(k) = \hat{C}^u(k) + \hat{C}^v(k)$	see Fig. 2.1	see Fig. 4.5

tial energy at scales larger than the deformation scale (Fig. 2.2).

Relation 2.4, however, does not holds for the three-dimensional internal-wave field. If the wave field is horizontally isotropic, as assumed in Garrett Munk (1972), the one-dimensional along-track and across-track kinetic energy spectra will be expected to be equal, $\hat{C}^u(k) = \hat{C}^v(k)$.

We summarize the above two main diagnostics, slopes and the ratio between along- and across track kinetic energy spectrum, and relations between potential and kinetic energy spectrum in Table 2.1. It provides insight for interpreting wavenumber spectra dominated by different types of motions. In particular, the ship track along- and across-track spectra are computed because their ratio is equal to their power law for non-divergent flow. Furthermore, using the Helmholtz decomposition as proposed by Bühler et al. (2014), a complex flow can be separated into various components. The power law of spectra, and the ratio of along-track and across-track are useful to diagnose whether observed flows are consistent with the theories presented in this chapter. Details of this method is presented in the next chapter.

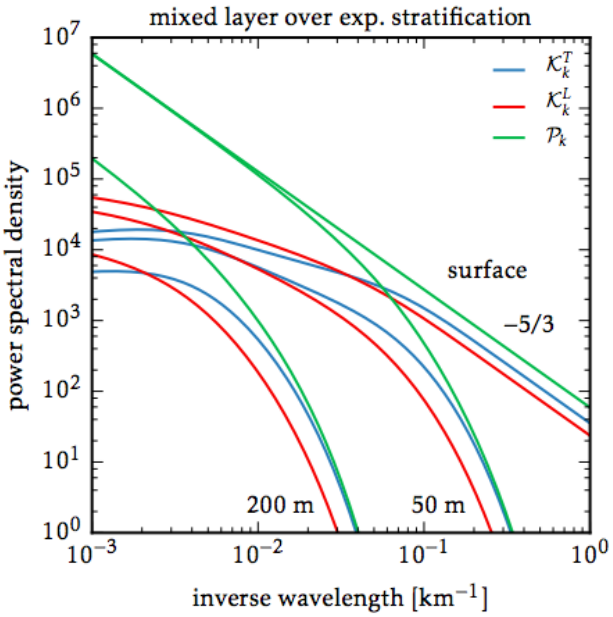

Figure 2.1: Surface QG predictions from Callies and Ferrari (2013) of two-dimensional isotropic wavenumber spectra of kinetic and potential energies for (a) constant stratification, (b) exponential stratification; green lines show potential energy and purple lines represent kinetic energy.

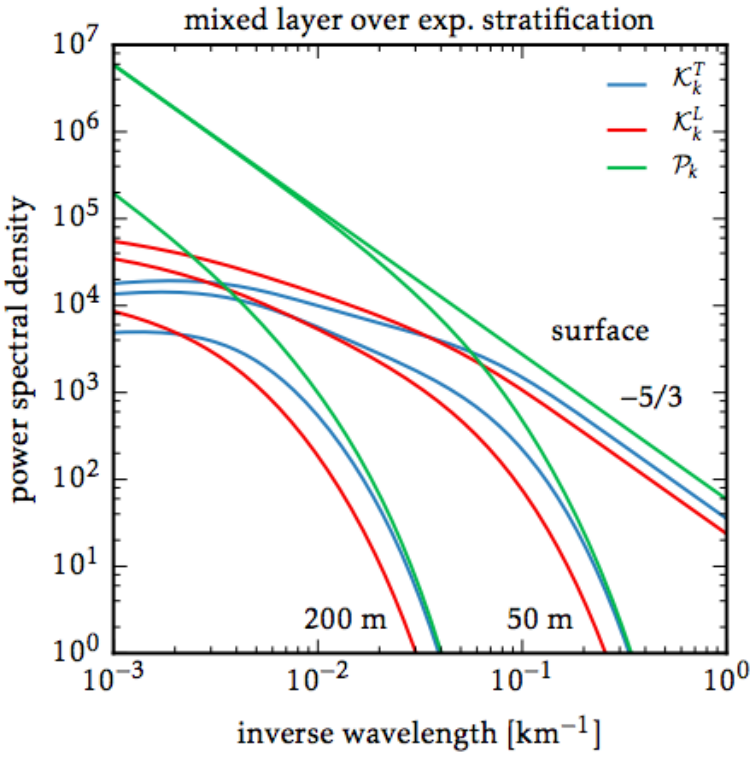

Figure 2.2: Surface QG predictions from Callies and Ferrari (2013) of one-dimensional wavenumber spectra of along- (L: longitudinal) and across (T: transverse) track kinetic energy and potential energy spectra.

Chapter 3

Review of Helmholtz decomposition

In this chapter, the method of Helmholtz decomposition to separate observed one-dimensional velocity spectra into non-divergent and divergent components (Bühler et al., 2014) is reviewed. Furthermore, the relative contributions of geostrophic eddies and internal waves (e.g. Bühler et al., 2014) are partitioned.

The method is based on the fact that QG motions are to first order non-divergent, and that by Helmholtz's theorem any two dimensional vector field can be decomposed into a non-divergent and divergent component. The statistics of the flow are assumed to be horizontally homogeneous and isotropic at the measured scales, and that their divergent and non-divergent components are uncorrelated. These assumptions allow us to consider flows that are purely non-divergent (Section 3.1.1) and divergent (Section 3.1.2) separately and add them together finally (Section 3.1.3). Decomposition is achieved by solving two simple ODEs in spectral space (numerical calculation is shown in Appendix A). While quasi-geostrophic motions are to leading order non-divergent, internal waves have both divergent and non-divergent components, the ratio of these elements are approximated from the GM model in order to uniquely decompose kinetic energy spectra (Bühler et al., 2014).

In Section 3.1, purely non-divergent and divergent solutions are introduced first and then the combined solution is shown. After that solutions for inertia-gravity waves are presented, followed by combination with a non-divergent flow in Section 3.2. In Section 3.3, two ways to achieve the second-step of Helmholtz decomposition are shown, one of which is observational buoyancy available and another one is to

approximate potential energy using the GM model. Summary is presented in the last Section.

3.1 Helmholtz decomposition

In order to apply the Helmholtz decomposition to the velocity field, the velocity with x aligned with the ship track is rotated, saying along-track (U) and across-track (V). Consider a standard flow that has both purely non-divergent and divergent components,

$$U = -\psi_y + \phi_x \quad and \quad V = \psi_x + \phi_y, \tag{3.1}$$

where $\psi(x, y)$ is a stream function due to non-divergent flows and $\phi(x, y)$ is a velocity potential due to divergent flows. If these two types of flows are uncorrelated, it is reasonable to consider them separately, non-divergent flow in Section 3.1.1, divergent flow in Section 3.1.2.

3.1.1 Solutions for non-divergent flows

First, if the flow is purely non-divergent, then $U_x + V_y = 0$, which allows us to express along-track velocity U and across-track velocity V by stream function $\psi(x, y)$ in a standard way:

$$U = -\psi_y;\ V = +\psi_x \tag{3.2}$$

Assuming ψ is a homogeneous and isotropic zero-mean random function,

$$E[\psi] = 0;\ C^{\psi}(x, y) = E[\psi(x_0, y_0)\psi(x_0 + x, y_0 + y)] = G(r) \tag{3.3}$$

where E denotes taking the expected value and $r = \sqrt{x^2 + y^2}, (r > 0)$. The function $G(r)$ is the covariance of the stream function, which is a function in the two-dimensional plane and includes all the statistical knowledge that is available for the random velocity field. $\hat{C}^{\psi}(k, l)$ is the Fourier transform of $C^{\psi}(x, y)$, i.e.

$$\hat{C}^{\psi}(k,l) = \int_{-\infty}^{\infty}\int_{-\infty}^{\infty} C^{\psi}(x,y)e^{-i(kx+ly)}dxdy = \hat{G}(k_h) \tag{3.4}$$

where $k_h = (k^2 + l^2)^{1/2}$. The corresponding non isotropic velocity spectra follow from 3.2 as

$$\begin{aligned} \hat{C}^{u}(k,l) &= l^2\hat{C}^{\psi}(k,l) = l^2\hat{G}(k_h) \\ \hat{C}^{v}(k,l) &= k^2\hat{C}^{\psi}(k,l) = k^2\hat{G}(k_h) \end{aligned} \tag{3.5}$$

Considering velocity along the ship track $y = 0 \quad and \quad r = x$, the corresponding power spectra can be achieved by integrating over the across-track wavenumber l:

$$\hat{C}^{\psi}(k) = \frac{1}{2\pi}\int_{-\infty}^{\infty} \hat{C}^{\psi}(k,l)dl = \frac{1}{\pi}\int_{|k|}^{\infty} \hat{G}(k_h)dl \tag{3.6}$$

Since $k_h = (k^2 + l^2)^{1/2}$, $ldl = k_h dk_h$ and $dl = \frac{k_h dk_h}{\sqrt{k_h^2 - k^2}}$ can be derived, which allows rewriting 3.6 as

$$\hat{C}^{\psi}(k) = \frac{1}{\pi}\int_{|k|}^{\infty} \frac{\hat{G}(k_h)}{\sqrt{k_h^2 - k^2}} k_h dk_h \tag{3.7}$$

The same steps lead to the one-dimensional velocity spectra from 3.5:

$$\psi \quad only : \hat{C}^u(k) = \frac{1}{\pi} \int_{|k|}^{\infty} \hat{G}(k_h) \sqrt{k_h^2 - k^2} k_h dk_h \tag{3.8}$$

$$\hat{C}^v(k) = \frac{k^2}{\pi} \int_{|k|}^{\infty} \frac{\hat{G}(k_h)}{\sqrt{k_h^2 - k^2}} k_h dk_h \tag{3.9}$$

where "ψ only" is added as a reminder that these expressions hold only for horizontally non-divergent flows that can be expressed through a stream function ψ. A useful relationship from 3.8-3.9 is obtained that has been noted in the last chapter (Charney, 1971):

$$\psi \quad only : \hat{C}^v(k) = -k \frac{d}{dk} \hat{C}^u(k) \tag{3.10}$$

For power-law velocity spectra of the form k^{-n} this yields

$$\psi \quad only : \hat{C}^v(k) = n \hat{C}^u(k) \tag{3.11}$$

3.1.2 Solutions for divergent flows

Considering a purely divergent flow in the same way as for the non-divergent flow above, such that 3.2 is replaced by

$$U = \phi_x;\ V = \phi_y \tag{3.12}$$

in terms of a homogeneous and isotropic zero-mean random potential function $\phi(x, y)$ defined by

$$E[\psi] = 0;\ C^{\phi}(x, y) = E[\phi(x_0, y_0)\phi(x_0 + x, y_0 + y)] = F(r) \tag{3.13}$$

where $F(r)$ is the covariance of potential ϕ. The same methods used in Section 3.1.1 for the non-divergent part, finally the one-dimensional ship track spectra can be expressed:

$$\phi \quad only : \hat{C}^u(k) = \frac{k^2}{\pi} \int_{|k|}^{\infty} \frac{\hat{F}(k_h)}{\sqrt{k_h^2 - k^2}} k_h dk_h \tag{3.14}$$

$$\hat{C}^v(k) = \frac{1}{\pi} \int_{|k|}^{\infty} \hat{F}(k_h) \sqrt{k_h^2 - k^2} k_h dk_h \tag{3.15}$$

where "ϕ only" is added as a reminder that these expressions hold only for divergent flows that can be expressed through a velocity potential ϕ. The relationship 3.10 is replaced by

$$\phi \quad only : \hat{C}^u(k) = -k \frac{d}{dk} \hat{C}^v(k) \tag{3.16}$$

and hence now the along-track spectrum dominates for power laws with n>1:

$$\phi \quad only : \hat{C}^u(k) = n\hat{C}^v(k) \tag{3.17}$$

Note that by definition both $\hat{G}$ and $\hat{F}$ are real and non-negative functions of k_h.

3.1.3 Solutions for combined divergent and non-divergent flows

Now, considering a general two-dimensional flow that has both non-divergent and divergent components, which can be expressed as:

$$U = -\psi_y + \phi_x \quad and \quad V = \psi_x + \phi_y, \tag{3.18}$$

which implies the two-dimensional Poisson equations

$$\psi_{xx} + \psi_{yy} = V_x - U_y \quad and \quad \phi_{xx} + \phi_{yy} = U_x + V_y \tag{3.19}$$

This means both ψ and ϕ are in fact determined by 3.19. Following Bühler et al. (2014), progress with the statistical theory is possible if ψ and ϕ are uncorrelated, i.e.

$$E[\psi(x_0, y_0)\phi(x_0, y_0 + y)] = 0 \tag{3.20}$$

Under this assumption, the covariances of the velocities associated with ψ and ϕ simply add up, yielding the one-dimensional ship-track spectra

$$\hat{C}^u(k) = \frac{1}{\pi}\int_{|k|}^{\infty}\left[\hat{G}(k_h)\sqrt{k_h^2-k^2} + \frac{k^2\hat{F}(k_h)}{\sqrt{k_h^2-k^2}}\right]k_h dk_h \tag{3.21}$$

$$\hat{C}^v(k) = \frac{1}{\pi}\int_{|k|}^{\infty}\left[\frac{k^2\hat{G}(k_h)}{\sqrt{k_h^2-k^2}} + \hat{F}(k_h)\sqrt{k_h^2-k^2}\right]k_h dk_h \tag{3.22}$$

These expressions can be substantially simplified if one introduces the auxiliary functions $D^{\psi}(k)$ and $D^{\phi}(k)$(Callies and Ferrari (2013))

$$D^{\psi}(k) = \frac{1}{2\pi}\int_{-\infty}^{\infty} l^2\hat{C}^{\psi}(k,l)dl = \frac{1}{\pi}\int_{|k|}^{\infty}\hat{G}(k_h)\sqrt{k_h^2-k^2}k_h dk_h \tag{3.23}$$

$$D^{\phi}(k) = \frac{1}{2\pi}\int_{-\infty}^{\infty} l^2\hat{C}^{\phi}(k,l)dl = \frac{1}{\pi}\int_{|k|}^{\infty}\hat{F}(k_h)\sqrt{k_h^2-k^2}k_h dk_h. \tag{3.24}$$

These functions D^{ψ} and D^{ϕ} are the spectra of ψ_y and ϕ_y, respectively, and they allow rewriting (3.21-3.22) in the form of

$$\hat{C}^u(k) = D^{\psi}(k) - k\frac{d}{dk}D^{\phi}(k) \quad and \quad \hat{C}^v(k) = D^{\phi}(k) - k\frac{d}{dk}D^{\psi}(k). \tag{3.25}$$

These two ordinary differential equation (ODEs) are the main result of this method, which incorporates both non-divergent and divergent special cases (solutions are shown in appendix A). In practice, this decomposes the total kinetic energy $KE = \frac{1}{2}[\hat{C}^u + \hat{C}^v] = \frac{1}{2}[K^{\psi} + K^{\phi}]$ into the non-divergent component, i.e

$$K^{\psi}(k) = \frac{1}{2}\left[D^{\psi} - k\frac{d}{dk}D^{\psi}(k)\right] \tag{3.26}$$

and the divergent component, i.e

$$K^{\phi}(k) = \frac{1}{2}\left[D^{\phi} - k\frac{d}{dk}D^{\phi}(k)\right]. \tag{3.27}$$

To this point, the total energy has been decomposed into non-divergent K^{ψ} and divergent K^{ϕ} components. In this thesis, this method will be applied to the velocities along Line P, and the divergent and non-divergent components are obtained. Inertia-gravity waves, however, have both divergent and non-divergent parts. So, a further step is needed to decompose kinetic energy spectra into wave and vortex constituents.

3.2 Combining inertia-gravity waves with QG flows

3.2.1 Inertia-gravity waves

Under the assumption that the waves are hydrostatic, the one-dimensional wave energy spectrum can be expressed by

$$E_W(k) = \frac{1}{2}\left[\hat{C}^u_W(k) + \hat{C}^v_W(k) + \hat{C}^b_W(k)\right], \tag{3.28}$$

where "W" denotes the wave component of the flow. Here $\frac{1}{2}\hat{C}^b_W$ is the spectrum of b/N, where b is the linear buoyancy disturbance, which is related to the vertical velocity w by $b + N^2 w = 0$. Hence $\frac{1}{2}\hat{C}^b_W$ is the potential energy spectrum. The calculation of $E_W(k)$ in 3.28 hinges on the following statement about energy equipartition for linear hydrostatic inertia-gravity waves that are stationary in time as well as spatially homogeneous in all the three directions: the sum of the potential energy plus the non-divergent horizontal kinetic energy due to ψ then equals the divergent

horizontal kinetic energy due to ϕ (Bühler et al. (2014), appendix 3.B), i.e

$$\hat{C}^b_W + \left[D^\psi_W(k) - k\frac{d}{dk} D^\psi_W(k) \right] = \left[D^\phi_W(k) - k\frac{d}{dk} D^\phi_W(k) \right]. \tag{3.29}$$

Substituting in 3.28, the key result is obtained:

$$E_W(k) = D^\phi_W(k) - \frac{d}{dk} D^\phi_W(k) \tag{3.30}$$

This relation is very useful, as wave energy is directly obtained from the power spectrum of D^ϕ. In the next section, following Bühler et al. (2014), ways to derive the balanced "vortex" part and unbalanced wave part are presented.

3.2.2 Combination with a non-divergent flow component

Allowing for the combination of inertia-gravity wave field with non-divergent flow, then the Helmholtz decomposition will be

$$\psi = \psi_W + \psi_V \quad and \quad \phi = \phi_W, \tag{3.31}$$

where the subscript V denotes the vortex part. The vortex part is horizontally non-divergent and therefore ϕ has no vortex part.

It is reasonable to assume that ψ_V is statistically independent of ψ_W and ϕ_W, in which case the covariances due to ψ_V simply add to the wave covariances, i.e.,

$$\hat{C}^u(k) = \hat{C}^u_W(k) + \hat{C}^u_V(k) \quad and \quad \hat{C}^v(k) = \hat{C}^v_W(k) + \hat{C}^v_V(k). \tag{3.32}$$

The corresponding Helmholtz decomposition yields

$$D^{\psi}(k) = D^{\psi}_{W}(k) + D^{\psi}_{V}(k) \quad and \quad D^{\phi}(k) = D^{\phi}_{W}(k) \tag{3.33}$$

such that

$$\hat{C}^{u}_{W}(k) = D^{\psi}_{W}(k) - k\frac{d}{dk}D^{\phi}_{W}(k), \quad \hat{C}^{v}_{W}(k) = -k\frac{d}{dk}D^{\psi}_{W}(k) + D^{\phi}_{W}(k) \tag{3.34}$$

$$\hat{C}^{u}_{V}(k) = D^{\psi}_{V}(k), \quad \hat{C}^{v}_{V}(k) = -k\frac{d}{dk}D^{\psi}_{V}(k) \tag{3.35}$$

The function $D^{\phi}_{W} = D^{\phi}$ is unaffected by the presence of the quasi-geostrophic flow and is calculated from the observed velocity spectra. At this point E_W, $D^{\phi} = D^{\phi}_{W}$ and the sum $D^{\psi} = D^{\psi}_{W} + D^{\psi}_{V}$ are known, but not D^{ψ}_{W} and D^{ψ}_{V} individually and hence not $\hat{C}^{u}_{V}$, $\hat{C}^{v}_{V}$ (3.35), which we want so we can check $\hat{C}^{v}_{V}/\hat{C}^{u}_{V} = R$. Bühler et al. (2014) proposed two options to solve the unknowns in (3.34-3.35): either from observing b/N along the ship track, or assuming additional information about the frequency content of the wave field.

3.3 Solutions with and without observational buoyancy spectrum

3.3.1 Solution using observed buoyancy spectrum

If buoyancy data (potential energy) is available along the ship track, then total energy spectrum can be calculated from the data (eq. 3.36).

$$E(k) = E_W(k) + E_V(k) = \frac{1}{2}\left[\hat{C}^{u}(k) + \hat{C}^{v}(k) + \hat{C}^{b}(k)\right] \tag{3.36}$$

E_W (eq. 3.30) is calculated by using the divergent part of the flow field from the Helmholtz decomposition, and hence the vortical component of the energy

$$E_V(k) = \frac{1}{2}\left[\hat{C}_V^u(k) + \hat{C}_V^v(k) + \hat{C}_V^b(k)\right] = E(k) - E_W(k), \tag{3.37}$$

and decomposed wave and vortical components.

Addititonal constraints on the spectra is needed to decompose the spectra into across- and along-track wave and vortical components ($\hat{C}_W^u$, $\hat{C}_W^v$ *and* $\hat{C}_V^u$, $\hat{C}_V^v$). Following Charney (1971),

$$\hat{C}_V^b = \hat{C}_V^u = D_V^\psi, \tag{3.38}$$

can be assumed.

Combining with 3.37 and 3.35, the known vortical spectrum in terms of the vortical part of D_V^ψ can be expressed:

$$\begin{aligned} E_V(k) &= \frac{1}{2}\left[D_V^\psi - k\frac{d}{dk}D_V^\psi(k) + D_V^\psi(k)\right] \\ &= D_V^\psi(k) - \frac{k}{2}\frac{d}{dk}D_V^\psi(k), \end{aligned} \tag{3.39}$$

which is an ODE for D_V^ψ in terms of $E_V(k)$. Knowing the vortical part of D_V^ψ, the wave part $D_W^\psi = D^\psi - D_V^\psi$ is known. Knowing the decomposition of D_W^ψ, $\hat{C}_W^u$, $\hat{C}_W^v$ *and* $\hat{C}_V^u$, $\hat{C}_V^v$ can be evaluated using equations 3.34 and 3.35.

3.3.2 Solution using the frequency model for the wave spectrum

Bühler et al. (2014) proposed a flexible modelling approach to approximate f^2/ω^2 as a function of $f^2/\omega_*^2(k)$, i.e

$$D_W^\psi(k) = \frac{f^2}{w_*^2(k)} D^\phi(k), \tag{3.40}$$

where ω_* is frequency as a function of wavenumber k. $\frac{f^2}{\omega_*^2(k)}$ (Appendix A.2) is estimated by the Garrett Munk model. With D_W^ψ and $D_V^\psi = D^\psi - D_W^\psi$ now in hand, expressions of wave and vortex constituents in (3.34-3.35) become

$$\hat{C}_W^u(k) = \frac{f^2}{w_*^2(k)} D^\phi(k) - k\frac{d}{dk} D^\phi(k), \quad \hat{C}_W^v(k) = -k\frac{d}{dk}\left[\frac{f^2}{w_*^2(k)} D^\phi(k)\right] + D^\phi(k) \tag{3.41}$$

$$\hat{C}_V^u(k) = D^\psi(k) - \frac{f^2}{w_*^2(k)} D^\phi(k), \quad \hat{C}_V^v(k) = -k\frac{d}{dk}\left[D^\psi(k) - \frac{f^2}{w_*^2(k)} D^\phi(k)\right]. \tag{3.42}$$

$\hat{C}_W^b$ can then be computed from 3.28, which provides a prediction for the buoyancy spectrum.

In conclusion, the two step of Helmholtz decomposition can separate arbitrary velocity spectra into vortical and wave components with buoyancy data; this method can also be achieved by using a wave model for the ratio between $\hat{D}_W^\psi(k)$ and $\hat{D}_W^\phi(k)$, even in the absence of buoyancy data. Of course, the latter modelled step is an approximation that really requires more empirical tests. This complete decomposition method is applied to in-situ and simulation data sets. Results and comparison are shown in chapter 5.

3.4 Summary of the Helmholtz decomposition method

The goal of the decomposition is to decompose along- and across-track spectra each into internal wave and "vortex" components. Helmholtz decomposition can decompose the observed along-track $\hat{C}^u$ and across-track $\hat{C}^v$ velocity spectra into non-divergent D^ψ and divergent D^ϕ components. Moreover, the function D^ϕ implies the energy spectrum E_W for hydrostatic inertia-gravity waves, and this implication is unaffected by the presence of a quasi-geostrophic vortex flow component. Additional buoyancy data allow us to compute the residual vortex energy spectrum E_V by simply subtracting the wave energy E_W from the total energy. Finally, if buoyancy data is not available, the GM model is used for the frequency content of the wave field to estimate the ratio of D^ψ_W to D^ϕ_W, and hence back out the flow components.

Chapter 4

Data and processing

In this chapter, data processing for the in-situ velocity measurements and NEMO3.1 simulation are described. Helmholtz decomposition is applied to these data in the next chapter.

4.1 Observational data set

Acoustic Doppler Current Profiler (ADCP) data collected along Line P (Fig. 1.1) with four transects in February and three in June during 2013-2015. These seven transects have data along the whole Line P covering about 1400km. Here, data processing of the February 2014 transect is presented as an example.

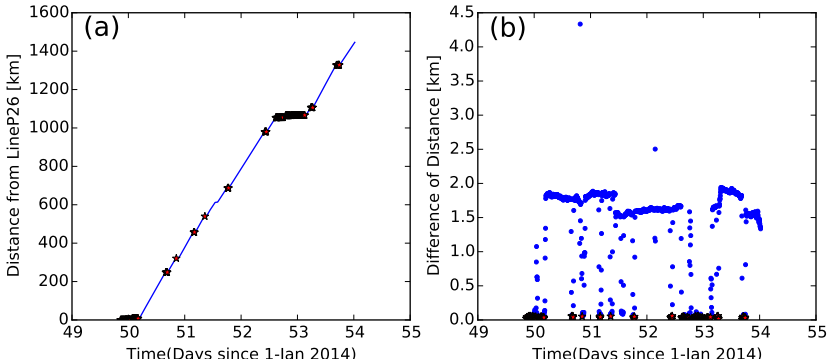

Figure 4.1: (a) Distance from station P and (b) difference between two pings versus time in February 2014. Red stars show the time when the ship is assumed to be deviating from the Line P (green line in Fig. 4.2).

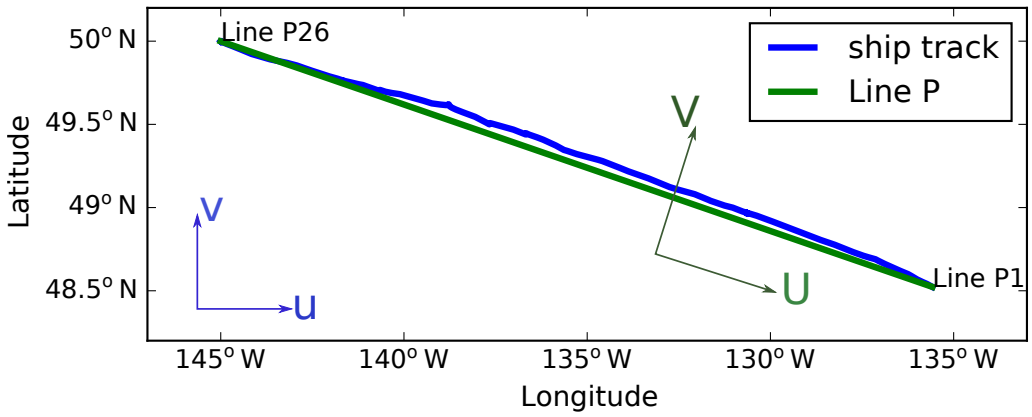

Figure 4.2: Ship track (blue line) and rotating transection (green line), on which observed velocities are interpolated

4.1.1 Data processing

The ADCP data were processed using the Common Ocean Data Access System (CODAS; Firing et al. 2012). In short, the ship-relative currents are rotated from ship-frame of reference to a geographic frame using the ship's gyro-compass. Before spectra analysis, the data where the ship stops or deviates from the course (red stars in Fig. 4.1a) need to be removed. The ship is assumed to have deviated from the course if the distance between two pings is less than 60 m (red stars in Fig. 4.1b). The threshold of 60 m is reasonable because the mean spacing of the raw data is approximately 1.5 km. Ocean current velocity was obtained by removing the ship's speed from the raw data measured by ADCP. The ship takes $\sim$ 3 days to travel the line ($\sim$1400 km) at a ship speed of 5 m/s. The common fast-tow assumption is assumed, i.e. the fields are frozen within the time over the course of a transect (e.g. Callies and Ferrari, 2013, Rocha et al., 2016). Geostrophic eddies have generally longer time scales (e.g Stammer, 1997) and are well-resolved. High-frequency internal wave component project onto small horizontal scales. The approximation becomes aliased for internal tides with large horizontal scales.

For each transect, at each depth, the ocean current velocity are interpolated from ship track onto Line P (green line in Fig. 4.2), and a horizontal grid for which the space is the same as the mean horizontal spacing of the ship track, approximately 1.5 km. Velocities have a lot of spikes that are removed before power spectra are calculated. The data are then interpolated onto a 750 m lateral grid to get the final ocean

current velocity. In order to use the Helmholtz decomposition, the velocity at each depth is rotated to the coordinate system with x aligned with Line P (Fig. 4.3). All power spectra are based in this frame, with $\hat{C}^u$, $\hat{C}^v$ and $\hat{C}^b$ (available in the simulation only) denoting along-track, across-track kinetic energy spectra and buoyancy spectra, respectively.

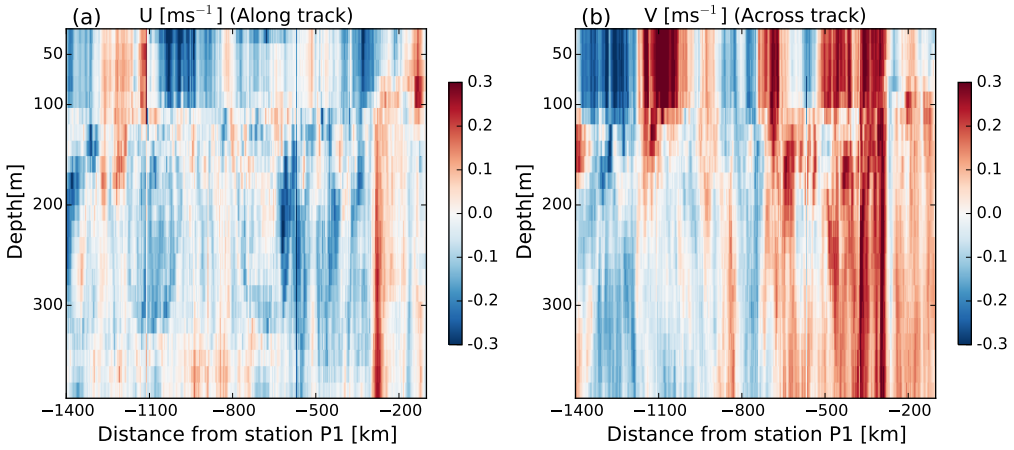

Figure 4.3: Observed velocities along track (U) and across-track (V) in February 2014.

4.1.2 Power spectra

Power spectra are calculated from discrete Fourier transforms of U and V at each depth by dividing into twelve segments at scales smaller than 33 km and into four segments at scales larger than 33 km, both with a 50%-overlap Hanning-window. The resulting Fourier transforms are averaged over the separate segments. After power spectra for each transect are calculated, power spectra for February are computed by averaging all transects for each time period (Fig. 4.5). Confidence intervals are determined from the chi-squared distribution for which the degrees of freedom are calculated from the number of overlaps in the windowed segments and the number of spectra.

Helmholtz decompositions are performed on the averaged power spectra. The two power spectra are merged onto a wavenumber grid of 0.001 cpkm for applying the Helmholtz decomposition (Fig. 4.4). Spectra at scales larger than 0.2 cpkm are truncated because spectra over this scales are aliased by the interpolation.

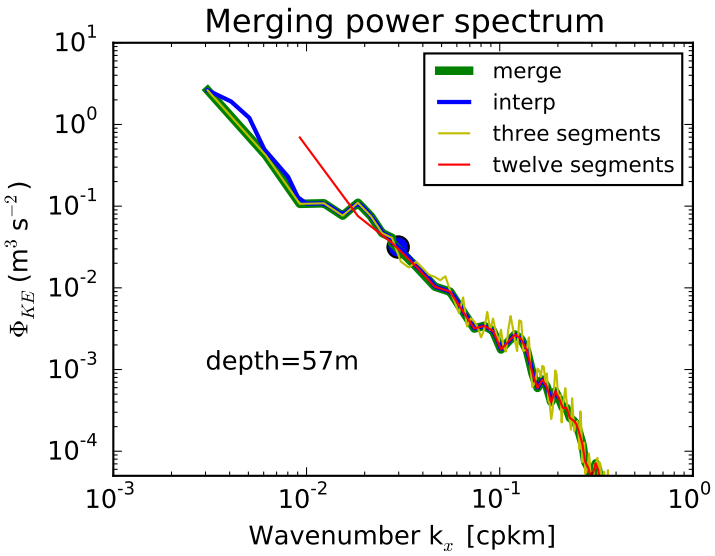

Figure 4.4: An example showing power spectrum merging and interpolation.

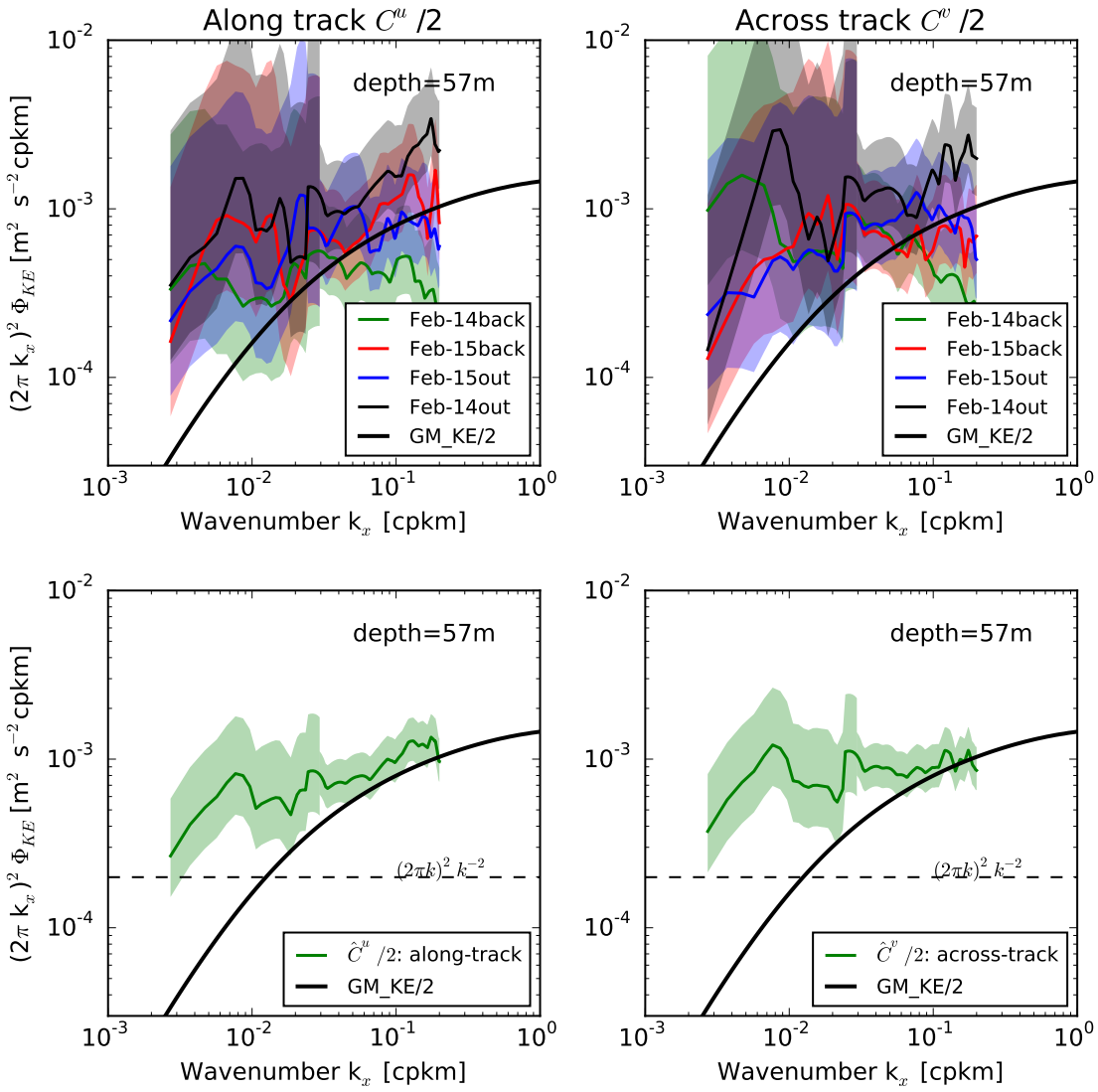

Figure 4.5: The upper panel shows spectra (whitened by $(2\pi k_x)^2$) of along- and across track for each transect in February at 57 m depth 2014-2015, (back means the ship goes from Station P to station P1, out means the ship goes from station P1 to Station P) The lower panel shows the averaged spectra of along- and across track.The shadings show 95 % confidence intervals; the GM model spectra for kinetic energy with black thick line; lines with slopes -2 and -3 for reference (dashed lines).

4.2 Simulation data set

The output from the $1/36^o$ (approximately 2.2 km) NEMO simulation (Zhai et al., 2015) are compared to the observations. Details of simulation set up can be found in Zhai et al. (2015). The simulation uses a scale-selective bi-harmonic operator to parameterize the horizontal mixing of momentum; the lateral mixing coefficient is $10^9 m^4 s^{-3}$. The simulation is forced by hourly atmospheric forcing, which is taken from a hindcast from the operational Global Deterministic Prediction System of the Canadian Meteorological Centre (Smith et al., 2014). This simulation takes lateral boundary conditions from the 2-day averaged coarse simulation (6.5 km) in a one-way nested fashion. Zhai et al. (2015) have shown that the simulation solutions are extremely sensitive to the value of the bi-harmonic viscosity and that the simulation output underestimates the eddy kinetic energy of surface geostrophic currents by 30 % with respect to the eddy kinetic energy derived from along-track altimeter data (Zhai et al., 2015). The simulation output is integrated with a time step of 60 s to get the hourly data set in February 2014.

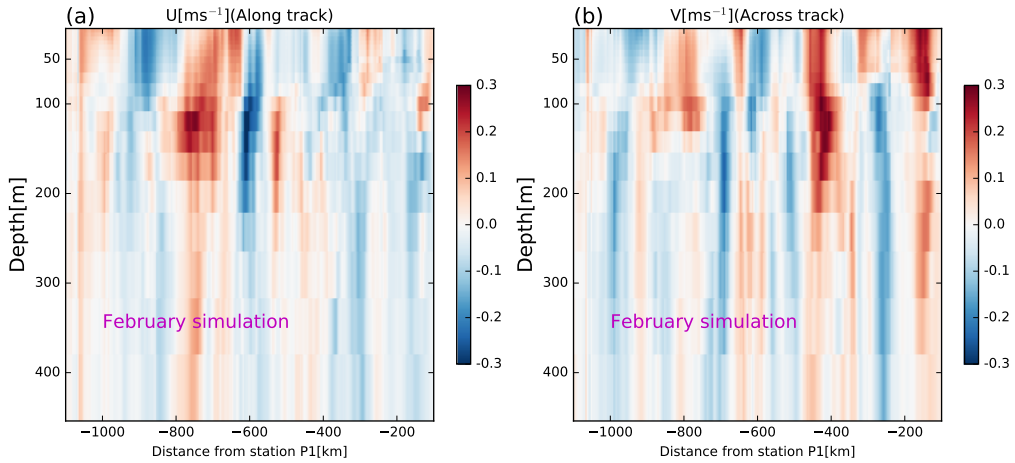

Figure 4.6: Along-track (U) and across-track (V) velocities from simulation, which are sampled along Line P according to the location of time of the shipboard ADCP.

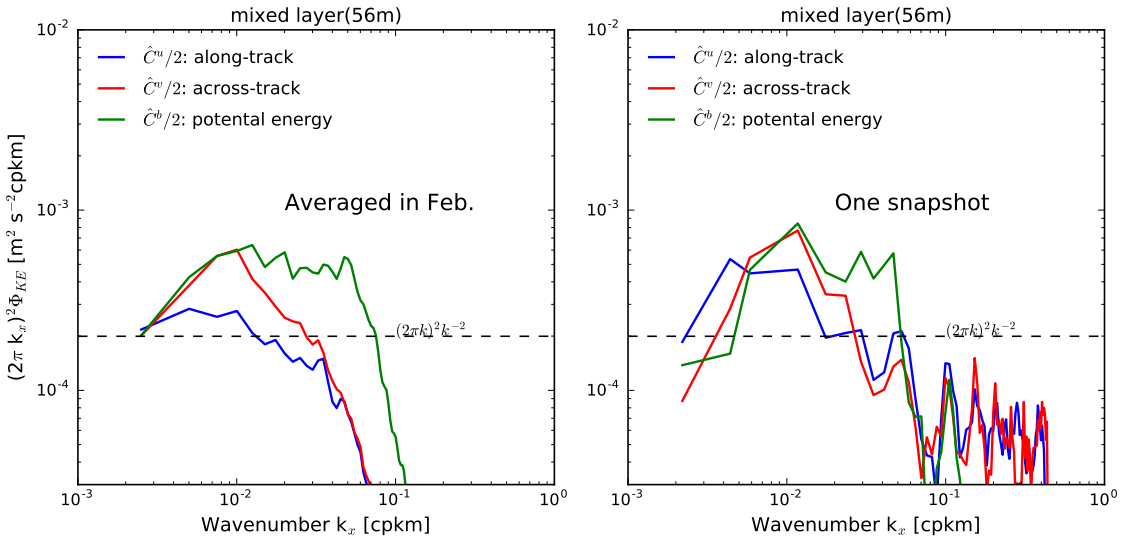

Figure 4.7: Power spectra (whitened by $(2\pi k_x)^2$) of along-, across-track kinetic energy and potential energy at depth of 56 m from simulation that are (a) averaged hourly spectra in February 2014 and (b) sampled according to the location of the shipboard ADCP.

4.2.1 Power spectra of simulation data

Spectra from the simulation are calculated by averaging the spectra of 720 snapshots in February. One snapshot in February are shown in Fig. 4.6. For each snapshot, at each depth, velocities from the frame of the earth coordinate are rotated to an along-track coordinate system, with x aligned with the ship track. Discrete Fourier transform of each snapshot are then calculated by dividing into five segments at scales smaller than 33 km and into two segments at scales larger than 33 km, both applying 50 % overlapping and a Hanning-window. The degrees of freedom is about 40 based on the time scales of de-correlation and the number of spectra.

Spectra from the simulation (Fig. 4.7) are quite different to the spectra from observations in the mixed layer. In particular, slopes are steeper than the observational spectra and roll off steeply at smaller scales. High viscosity is the most likely possibility that leads to the steep slope. Another difference is that kinetic energy spectra are lower than the observations. This is likely induced by the input forcing for the simulation, like winds.

4.3 Summary

In this chapter, data processing for the data from in-situ measurements and NEMO3.1 simulation described. In particular, kinetic energy spectra are calculated by averaging available transects, three transects in June and four transects in February. For NEMO simulation, the kinetic energy spectra are obtained by averaging the spectra for each hour in February.

Decomposing energy into wave and vortex components is a useful tool. The balanced vortex component can be compared with the quasi-geostrophic turbulence theory to figure out if the the flow is consistent with the existing theory. In addition, the wave constituents can be compared with the empirical GM model to diagnose if the wave component is dominated by internal waves or other unbalanced motions. Decomposition of the data is shown in detail in the next chapter.

Chapter 5

Results

In this chapter, the kinetic energy spectra are used to indicate that a balanced flow is dominant in the Line P data set at scales between 40 and 100 km while internal waves are more energetic at small scales. There is no evidence of depth variability, which is inconsistent with the surface QG theory. In the NEMO3.1 simulation, there is no evidence of internal waves but as in the observations there is a balanced flow at scales larger than 40 km. Depth trends of decomposed vortical motions from the simulation are consistent with predictions of depth variability in the surface QG theory.

5.1 Spectra comparison between simulation and observations in the mixed layer

5.1.1 Energy spectra in the mixed layer

In the mixed layer, high frequency internal waves are not energetic and thus vertical motions are weak. In winter time, the mixed layer depth (MLD) along Line P can be deeper than 100 m (Klymak et al., 2015); kinetic energy spectra at a depth of 57 m in February (Fig. 5.1a) and 25m in June (Fig. 5.1b) are presented to make sure they are within the mixed layer. For the NEMO February simulation data(Fig. 5.1c), spectra at 56 m are considered.

In February, the data indicate that the flow is neither purely internal waves nor purely non-divergent vortical motions (Fig. 5.1a). The along-track $\hat{C}^u$ and across-track $\hat{C}^v$ kinetic energy approximately follow a power law of k^{-2} between 10 and 100 km. The high wavenumber limit of 10 km is chosen because smaller than which

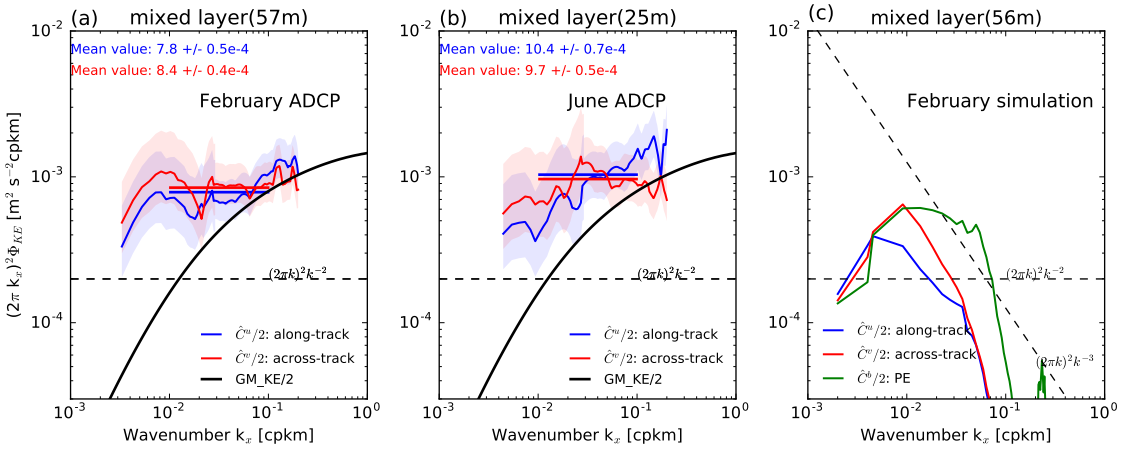

Figure 5.1: Along-track (blue lines) and across-track (red) kinetic energy in the mixed layer in (a) February, (b) June and (c) simulation, together with potential energy (green line). Mean values of energy are calculated by averaging the observational energy between 1/10cpkm and 1/100 cpkm in (a). The Garrett and Munk internal wave spectrum is indicated with the thick black lines. Spectra have been whitened by multiplying $(2\pi k_x)^2$.

the kinetic energy spectra become comparable with the GM model, i.e., the quasi-geostrophic theory does not apply at these scales anymore. The amplitudes of the across- and along-track spectra are approximately equal, i.e. $R \simeq 1$. If these scales were dominated by purely two-dimensional non-divergent motion with a spectral slope of -2, relation 3.10 predicts $R = 2$. Therefore internal waves are likely important at these larger scales. Kinetic energy spectra compare well with the GM model at scales smaller than 25 km.

In June, the mixed layer shoals, so we consider kinetic energy spectra at 25 m (Fig. 5.1b). The flows are similar to February though the slopes of the the along-track $\hat{C}^u$ is more blue than the across-track $\hat{C}^v$. The ratio of $\hat{C}^v$ and $\hat{C}^u$ is approximately 1, which is not equal the exponent of kinetic energy spectra, indicating internal waves also play a role in June. At large scales, the amplitudes of kinetic energy in June are slightly smaller than in February whereas internal waves are slightly stronger than in February over scales smaller than 1/25 cpkm.

Spectra from the simulation (Fig. 5.1c) indicate that motions of non-divergent vortical flow are not as energetic as the observations, and that there is no evidence of internal waves. Between 25 and 100 km, $\hat{C}^v$ is greater than $\hat{C}^u$, but the lack of a

clear power law in the spectra makes assessing the energy ratio complicated. There is a peak in the kinetic energy at around 100 km. The potential energy spectra follow a power law of k^{-2} between 100 and 10 km. One obvious difference between simulation and observations is that internal waves are weak in the simulation. The energy falls off steeply at scales smaller than around 25 km and the wave spectra from simulation are not comparable with the GM model.

There are several possibilities explain for the steep slope in the simulation. For example, high biharmonic viscosity will lead to energy dissipating more quickly.

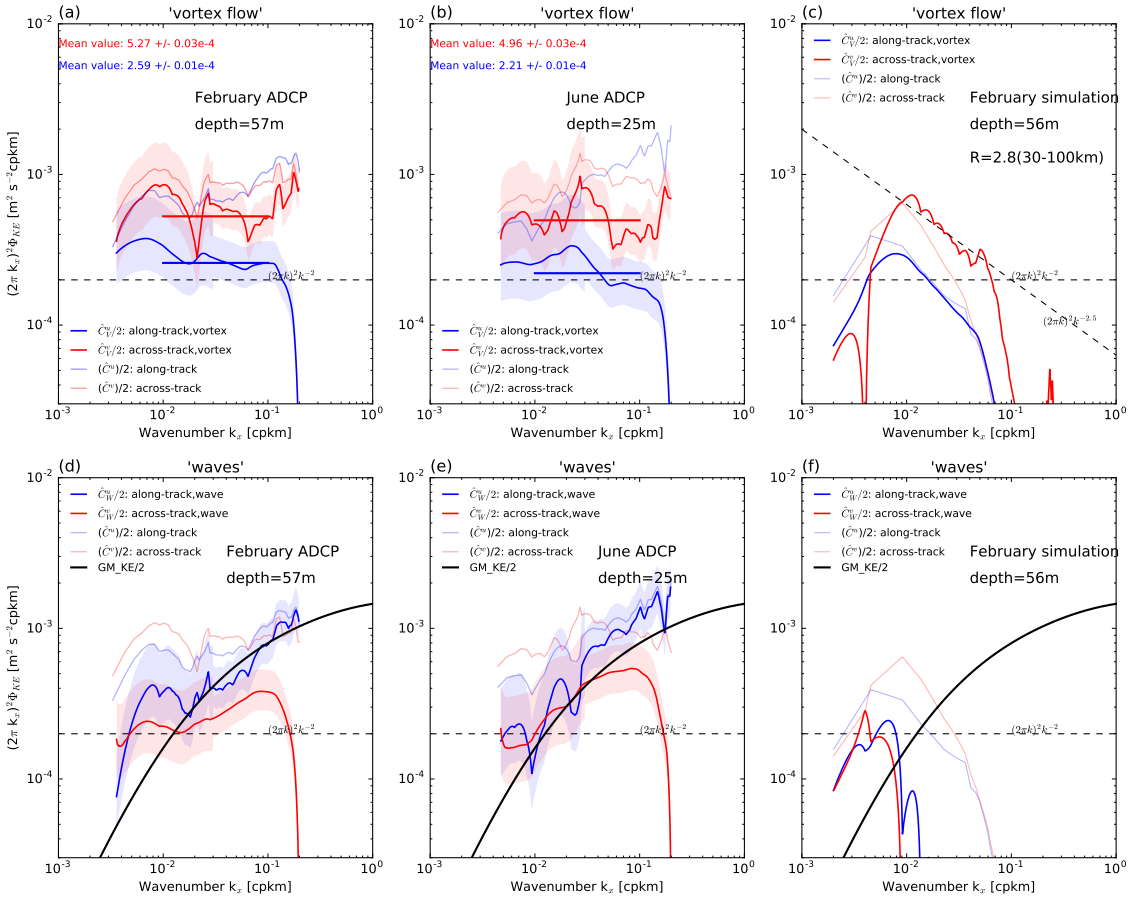

Figure 5.2: Decomposition into vortex (a, February; b, June; c, simulation) and waves (d, February; e, June; f, simulation). Mean values of energy are calculated by averaging the energy between 10 (0.1) and 100 (0.01 cpkm) km for observational energy in (a) and (c). The GM spectrum indicated by the thick black lines is plotted in the wave figures for reference. Spectra have been whitened by multiplying $(2\pi k_x)^2$. In (a)-(b) and (d)-(e), shades represent 95% confidence limits.

In the observations, there is likely substantial overlap in the internal wave and vortical motions, particularly at large scales. Following Bühler et al. (2014), kinetic energy spectra are decomposed into vortical and wave component to get a better idea of the power law and behaviour of the two flow components.

5.1.2 Decomposed mixed-layer vortex and wave kinetic energy spectra

Decomposing the February data into vortex (Fig. 5.2a) and wave components (Fig. 5.2d) show that the spectra are dominated by internal waves at scales smaller than 25 km, with evidence of dominance by a two-dimensional non-divergent flow at scales larger than 40 km. Vortex component from both along-track ($\hat{C}_V^u$) and across-track ($\hat{C}_V^v$) have power laws of k^{-2}. Calculating the mean energy between 10 and 100 km and showed that the amplitude of $\hat{C}_V^v$ approximately twice $\hat{C}_V^u$. The ratio of decomposed across- and along-track kinetic energy spectra are not sensitive to the higher wavenumber limit ($R_{Feb} \simeq 2.14, R_{Jun} \simeq 2.27[15-100km]; R_{Feb} \simeq 2.18, R_{Jun} \simeq 2.37[20-100km]; R_{Feb} \simeq 2.15, R_{Jun} \simeq 2.24[25-100km]$). The ratio of $\hat{C}_V^v$ and $\hat{C}_V^u$ is equal the exponent of the slopes, suggesting that the decomposed vortex flow is indeed a non-divergent flow. Decomposed wave energy are consistent with the GM spectrum at scales smaller than roughly 100 km. However, internal wave energy was not equipartitioned between along- and across-track, with twice the wave energy in along-track than across-track. We also note that energy is larger than the GM spectra at scales greater than 100 km. The disagreement with GM at large wavelengths could be because of imperfection in the decomposition technique. It is also possible that the wave field does not exactly follow the GM spectrum at these wave numbers. The vertical displacement spectrum observed on this line (from different cruise) had a similar deviation from the GM model at low (<1/50 cpkm) wave numbers (Klymak et al., 2015).

Vortex motions in June (Fig. 5.2b) have lower energy in the non-divergent flow than February at scales larger than 40 km, and slightly stronger internal waves at scales smaller than 25 km. Both the slopes (-2) of the vortex kinetic energy and the ratio of $R = \hat{C}_V^v/\hat{C}_V^u \simeq 2$ are the same as that shown in February between 10 and 100 km. However, mean energy in this range is slightly weaker than in February. Amplitudes of energy fall off quickly below the scale of 100 km. In addition, internal waves in June (Fig. 5.2e) are slightly stronger at scales smaller than 25 km, but not

so energetic at large scales as February.

In the simulation, non-divergent motions (Fig. 5.2c) are slightly lower than that in February from observations at scales larger than 40 km, with deeper slopes. At scales between 25 and 100 km, the vortex components follow power laws of $k^{-2.5}$, the exponent of which is close to the ratio of $\hat{C}_V^v/\hat{C}_V^u \simeq 2.8$, indicating a non-divergent flow. Wave energy is negligible in the simulation.

All the analysis above focuses on one depth in the mixed layer, depth trend of spectra are also analyzed in the next section.

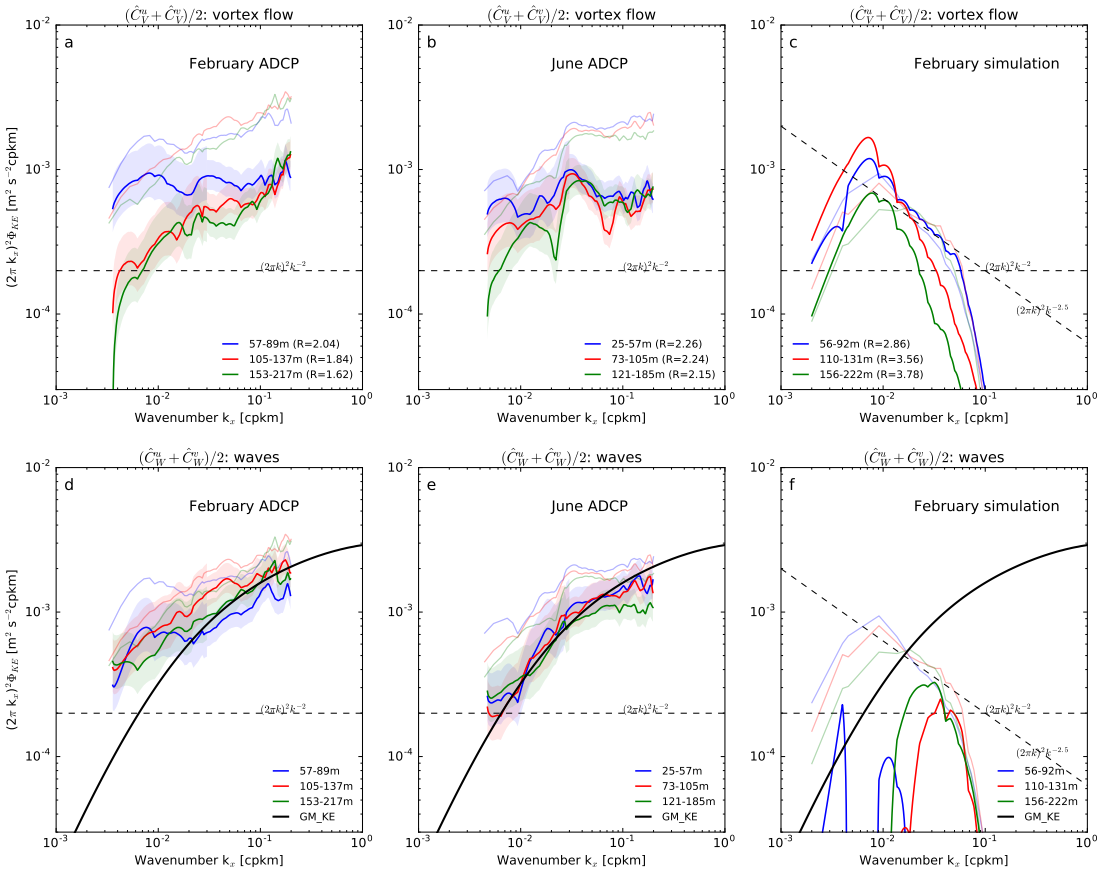

Figure 5.3: Wave-vortex decomposition in (a-vortex, d-wave) February, (b-vortex, e-wave) June and (c-vortex, f-wave) simulation. Lines with light color are the total kinetic energy in each depth bin. R is the ratio of across-track to along-track vortex kinetic energy. The GM indicated by the thick black lines spectrum is plotted in the wave figures for reference. Spectra have been whitened by multiplying by $(2\pi k_x)^2$. Shadings are 95 % confidence limits.

5.2 Depth trends in spectra

In February, depth trends of vortex kinetic energy show that non-divergent vortical flow (Fig. 5.3) decreases with depth over small wave numbers (< 1/50 cpkm) with no evidence of surface QG turbulence, whereas internal waves do not show depth dependence. At scales between 10 and 100 km, the kinetic energy spectra near the surface follow power laws of approximately k^{-2}, the exponent of which is very close to the ratio of $R = \hat{C}_V^{\psi}/\hat{C}_V^{\phi}$ (averaged between 10 and 100 km), indicating the flows are non-divergent. Kinetic energy of this vortical non-divergent flow decreases and is bluer (more wavenumber variance) with depth at low wave numbers (<1/50 cpkm), which is similar to the roll-off trend of kinetic energy predicted by (Callies and Ferrari, 2013) for flows with non-constant stratification. At high wave numbers, however, no evidence of depth dependence is found, which is inconsistent with the surface QG turbulence theory that predicts steeper spectra with depth. In addition, surface QG theory predicts that spectra follow a slope of -5/3 at the surface, which is different to our observed slopes (-2). However, surface QG has been revised after the ageostrophic flows are included (Boyd, 1992) to the idealized surface QG flow and predicts that the slope of spectra become -2. Thus, divergent ageostrophic flows might play a role. Besides the balanced flow, internal waves account for a large part of energy at all scales, even at scales larger than 100 km, and their amplitude is independent of depth. This can be due to the large scale of inertia-gravity waves, like the internal tides. In all, it is shown that the near-surface balanced motions along Line P in February are not fully inconsistent with the predictions of surface QG theory, and that the internal waves are energetic at all scales and independent of depth.

Motions in June exhibit almost the same patten as that in February, with a slightly lower energy of both the balanced flow and internal waves. Kinetic energy spectra (Fig. 5.3b) follow a slope of -2 at scales smaller than 50 km. In addition, at low wavenumbers, the amplitudes of spectra are smaller in June than in February. The kinetic energy spectra do not steepen with depth as predicted by surface QG. Internal waves (Fig. 5.3e) do not show depth variability either.

In the simulation, depth trends of non-divergent flow have characteristics consistent with a surface QG flow. Decomposed vortex spectra show a slope of -2.5 at near-surface and become steeper between 25, the smallest resolvable scale, and 100 km. The amplitudes of the kinetic energy spectra decrease with depth in this range, which is in agreement with the predictions of depth variability in the surface QG

Table 5.1: The slopes of decomposed vortex component and the ratio of along-track $\hat{C}_V^v$ and across-track $\hat{C}_V^u$ kinetic energy from observations and simulation in the mixed layer. Comparison with the GM model and depth variability are also show.

	Variables \ Dataset	Feb. (ADCP)	Jun. (ADCP)	Feb. (simulation)
Vortex	slope	-2 (30-100 km)	-2 (30-100 km)	-2.5 (30-100 km)
	Ratio=$\hat{C}_V^v/\hat{C}_V^u$	2	2	2.8
	depth variability	yes ($\geq 100km$)	yes ($\geq 100km$)	yes (25-100 km)
Waves	Match with the GM spectrum	yes ($>$ 50 km)	yes (all scales)	no
	depth variability	no	no	no

theory.

5.3 Summary

The wave-vortex decomposition and depth trend from the observations and the simulation are summarized in Table 5.1. Motions along Line P are the combination of balanced non-divergent flow and internal waves between 10 and 100 km. At low wave numbers ($<$ 1/100 cpkm), amplitudes of kinetic energy spectra of non-divergent flow become flatter and decreased with depth. However, at high wavenumbers, the vortical part of the spectra do not show a depth dependence, whereas if the flow were consistent with surface QG we would expect them to steepen with depth. The slopes of kinetic energy spectra are approximately -2 and inconsistent with slopes (-5/3) predicted by the surface QG theory, indicating that ageostrophic flows likely play a role. Internal waves also show little depth variability and match well with the GM model at scales larger than 25 km. Decomposed waves from observations have a good agreement with the GM spectrum, with little depth variability. In all, both vortex and wave energy in February are slightly larger than that in June.

In the simulation, kinetic energy spectra have steeper slopes (-2.5) compared with the slope of -5/3 predicted by the surface QG theory. In addition, the kinetic energy

spectra roll off steeply over high wavenumbers, which is likely induced by the high biharmonic viscosity. The depth trend of the non-divergent flow also shows roll-off and high-wavenumber steepening. Compared with observations, wave energy spectra from simulation do not compare well with the GM spectrum, indicating no evidence of internal waves.

Chapter 6

Conclusions and Discussion

6.1 Conclusion

In this thesis, kinetic energy spectra using data from in-situ measurements along Line P in the Northeast Pacific and a NEMO3.1 $1/36^o$ simulation are analyzed. Following (Bühler et al., 2014), the method of Helmholtz decomposition was used to decompose the kinetic energy into vortex and wave components. Spectra of decomposed vortex flow from along-track ($\hat{C}_V^v$) and across-track ($\hat{C}_V^u$) follow power laws of k^{-2} between 40 and 100 km, with the ratio of $\hat{C}_V^v/\hat{C}_V^u$ to be approximately 2, which is consistent with predictions of a non-divergent flow. Our main finds are:

- **Seasonal changes of balanced flows:** Balanced non-divergent flows are slightly more energetic in February than that in June in the mixed layer.
- **Inconsistency with surface QG:** Depth variability of non-divergent vortical flows show that at low wave-number energy decreases and is bluer with depth as predicted by surface QG theory. However, no evidence of high-wavenumber steepening with depth was found.
- **Consistency with the Garrett Munk model:** Wave components compare well with the GM spectrum over all scales in June, with higher level of energy at low wave numbers (<1/50 cpkm) than the GM model in February. Internal waves are slightly more energetic at scales smaller than 25 km in June than in February. Little depth variance of internal waves is found.
- **Comparison between observations and simulation**: In the simulation, balanced non-divergent flows are not as energetic as the observations, with no

evidence of internal waves. Slopes of kinetic energy spectra are steeper than the observations. In addition, the depth variance of the vortex component show that the kinetic energy spectra fall off steeply and decrease with depth between 25 km and 100 km, which is consistent with the predictions of surface QG turbulence for depth variability.

6.2 Discussion

A possible issue with the present results is the fidelity of the decomposition, which relies on the assumptions that the flow statistics are stationary, horizontally homogeneous, and isotropic. Another less obvious restriction of would be the impact of correlations. The assumptions of uncorrelated divergent ϕ and non-divergent ψ, which underly both steps, presumably would fail for waves with a noticeable vortex component. Last, in applying the second step of the decomposition, the GM model was used to simulate the ratio of ψ/ϕ in the inertia-gravity wave spectrum. If the actual internal wave field had a significantly different frequently content than Garrett Munk (for instance a strong tidal peak), then this step in the decomposition may not be entirely accurate. This assumption could be tested in cases where buoyancy data is available. None of these assumptions are necessarily true in the real ocean. Furthermore, large error bars in the observed kinetic energy spectra reduce the confidence in our results. We have only four transects in February and three in June, leading to error bars that are rather large.

These caveats aside, we can compare our results to similar attempts to characterize the upper ocean kinetic energy. In the subtropical North Pacific, Callies and Ferrari (2013) showed similar kinetic-energy levels in the mixed layer and thermocline. Along- and across-track kinetic energy spectra had power laws of k^{-2}, as observed here. They suggested the inconsistency between the exponent of the power law and the ratio of $R = \hat{C}^v/\hat{C}^u \sim 1$ at scales larger than 20 km results from a flow that is partially horizontally divergent. Helmholtz decomposition was applied to these data sets and showed that the energy spectra were dominated by inertia-gravity waves at scales smaller than 100 km (Bühler et al., 2014). The depth variability of the vortical spectra are not examined by Bühler et al. (2014).

Slopes of kinetic energy spectra along Line P are flatter compared with observations where mesoscale energy is strong. In the Gulf Stream, Wang et al. (2010) obtained a k^{-3} kinetic energy spectrum between 10 and 150 km using a 10-yr (1994-

2004) repeat shipboard ADCP data set. Recently, Rocha et al. (2016) showed that kinetic energy spectra approximately follow power laws of k^{-3} between 10 and 200 km by analyzing 13-yr of shipboard ADCP measurements in Drake Passage and also found that the shape of the kinetic energy spectra was independent of depth. These characteristics resemble the predictions of interior QG turbulence. However, the ratio ($R \simeq 1.5 < 3$) between across- and along-track total kinetic energy significantly departs from the expectation of interior QG turbulence. After applying the Helmholtz decomposition to the ADCP data, Rocha et al. (2016) showed that decomposed vortical motions have a slope of -3 and $R \simeq 3$, consistent with interior QG prediction. They also performed Helmoholtz decomposition on a simulation output ($llc4320MITgcm$) and found that decomposed divergent, ageostrophic motions account for about 20% of kinetic energy at scales between 10 and 150 km, and they contain about half of the kinetic energy at scales smaller than 40 km.

Lateral spectra of spice along isopycnals allow inferences about the balanced part of the flow (Klymak et al., 2015) and can be compared with our vortex flows from ADCP measurements. Spice is a passive tracer, and when considered along isopycnals helps isolate the stirring signal from the action of internal waves. In constant stratification, surface QG theory predicts that power laws of surface tracer spectra are the same as kinetic energy spectra, following $k^{-5/3}$, and that the slopes of tracer spectra become flatter with depth (Scott, 2006).

There are similarities and differences between our observed kinetic energy spectra and observations of spice spectra along Line P (Klymak et al., 2015). We found higher kinetic energy level compared to the GM model at low wave numbers, which is consistent with lateral spectra of vertical displacements showed by Klymak et al. (2015). Both depth variability of the present kinetic energy spectra and spice spectra from Klymak et al. (2015) are inconsistent with predictions of surface QG. In particular, both kinetic energy spectra and spice spectra from Klymak et al. (2015) are the opposite of the prediction from surface QG of steeper spectra with depth. High-resolution fully non-linear numerical simulations have shown that nonlinear frontogenesis can explain steeper tracer-gradient slopes (Capet et al., 2008b, Klein et al., 2008). Klymak et al. (2015) showed more peaked distributions of tracer than a normal distribution, lending some evidence for the importance of frontal processes. However, Klymak et al. (2015) suggested that surface frontogensis could not explain all the variations with spice spectra because they did not find bluer slopes with depth, and also because the coherence of the spectra drop off rapidly in the vertical. Thus, more exploration

of the fate of stirring along isopycnals at Line P should help to discover what sets the spectra of kinetic energy at the ocean surface, which has not been fully answered yet.

Compared with other regions, the present observation show kinetic energy spectra have the same slope (-2) as the spice spectra (Klymak et al., 2015), which is inconsistent with surface QG theory. Previous observations of Cole et al. (2010) and Cole and Rudnick (2012) showed that slopes of passive-tracer spectra are close to -2 everywhere in the upper 1000 m in the subtropical North Pacific. Similar results are reported by Ferrari and Rudnick (2000) and Callies and Ferrari (2013), including a tow that followed an isopycnal, giving high-wave number information. These papers also point out that such a slope is inconsistent with surface QG theory, and suggest that stirring possibly created discontinuous fronts (Hoskins and Bretherton, 1972, Boyd, 1992). Callies and Ferrari (2013) reported depth independent of temperature spectra in the subtropical North Pacific, similar to the present observations of depth independent of kinetic energy spectra. In terms of seasonal changes, we found kinetic energy is slightly higher in February than in June in the mixed layer, is the opposite shown by the temperature spectra in the subtropical North Pacific as reported by Cole et al. (2010).

6.3 Future work

In this thesis, kinetic energy from observations with relatively large error bars are analyzed. If more ADCP measurements along Line P were available, the error bars could be reduced and results will be have more fidelity. The error bars of the decomposed components were not analyzed as they come from a wide variety of sources, like when solving the two ODEs in step one of Helmholtz decomposition. In addition, the GM model is used to simulate the potential energy when decomposing the kinetic energy spectra into wave and vortex energy spectra. If observational buoyancy data sets were available, decomposition from potential energy would thus be obtained, which could be used to test the GM model assumption.

Furthermore, the simulation also can be improved since we did not capture energy at high wave numbers. It is possible that the hyper bi-viscosity is higher than it needs to be in the model configuration used, and tests of changes to the power spectra at different values of the hyper viscosity would be interesting. However, kinetic energy spectra from NEMO3.1 simulation follow power laws of $k^{-2.5}$ between scales of 20 and 100 km, the exponent of which is steeper than the spectra (k^{-2}) from high-resolution

(0.75 km) simulation in the Regional Oceanic Modelling System (ROMS) (Capet et al., 2008a).

Appendix A

Appendices

A.1 Numerical calculation for two ODEs

Rewriting (3.25) into

$$\frac{dD^{\phi}}{dk} = \frac{D^{\psi}}{k} - \frac{\hat{C}^{u}}{k} \quad and \quad \frac{dD^{\psi}}{dk} = \frac{D^{\phi}}{k} - \frac{\hat{C}^{v}}{k} \tag{A.1}$$

combining the two equations in (A.1):

$$\frac{d}{dk}\begin{pmatrix} D^{\phi} \\ D^{\psi} \end{pmatrix} = \begin{pmatrix} 0 & \frac{1}{k} \\ \frac{1}{k} & 0 \end{pmatrix} \begin{pmatrix} D^{\phi} \\ D^{\psi} \end{pmatrix} + \begin{pmatrix} -\frac{\hat{C}^{u}}{k} \\ -\frac{\hat{C}^{v}}{k} \end{pmatrix} \tag{A.2}$$

Denote $D^{\phi} = x$, $D^{\psi} = y$, then it turns to:

$$X = \begin{pmatrix} D^{\phi} \\ D^{\psi} \end{pmatrix} = \begin{pmatrix} x \\ y \end{pmatrix} \tag{A.3}$$

(A.2) becomes:

$$func = \begin{pmatrix} f0 \\ f1 \end{pmatrix} = \frac{d}{dk}\begin{pmatrix} x \\ y \end{pmatrix} = \begin{pmatrix} 0 & \frac{1}{k} \\ \frac{1}{k} & 0 \end{pmatrix}\begin{pmatrix} X[0] \\ X[1] \end{pmatrix} + \begin{pmatrix} -\frac{\hat{C}^u}{k} \\ -\frac{\hat{C}^v}{k} \end{pmatrix} = \begin{pmatrix} \frac{1}{k}X[0] - \frac{\hat{C}^u}{k} \\ \frac{1}{k}X[1] - \frac{\hat{C}^v}{k} \end{pmatrix}. \tag{A.4}$$

With the initial condition:

$$y(k_\infty) = 0, \quad and \quad x(k_\infty) = 0, \tag{A.5}$$

we can solve (A.4) with Euler method. Specifically, we choose m for the size of the step and define $k_m = k_0 + m\Delta k$, then one step from k_n to $k_{m+1} = k_m + \Delta k f(k_m, y_m)$. Note that in order to get the precise numerical solution, we would decrease the step into $dk' = dk/4$. Finally, x and y can be solved. Note that during this numerical process, we can compare the real $\hat{C}^u$ and $\hat{C}^v$ with the numerical ones that are derived from $D\psi$ and $D\phi$ to check the numerical errors. Notably, during this process, there might lead to unphysical negative values in $D\psi$ and $D\phi$. This may occur when either $D\psi$ and $D\phi$ become very small, way comparable to the instrumental noise threshold or to the errors imposed by the limitations of the assumptions of isotropy and homogeneity in the data.

A.2 Garrett Munk model for D^ψ/D^ϕ

In 1991, Garrett Munk gives an empirical expression for the total energy spectrum, which depends on frequency (ω) and vertical wavenumber (k_z).

$$E_{GM}(\omega, j) = E_0 B(\omega) H(j), \tag{A.6}$$

where E_0 is a constant;

$$B(\omega) = C\frac{2f}{\pi\omega}(\omega^2 - f^2)^{-1/2}, \quad \int_f^N B(\omega)d\omega = 1 \tag{A.7}$$

where C is a normalization constant, i.e.

$$C(j) = 1/(\int_f^N \frac{2f}{\pi\omega}(\omega^2 - f^2)^{-1/2})d\omega \tag{A.8}$$

and

$$H(j) = \frac{(j^2 + j_*^2)^{-1}}{\sum_1^{j_{max}}(j^2 + j_*^2)^{-1}}. \tag{A.9}$$

Here, j_* is a parameter in the GM model and was chosen to be 3. j is the mode number, which relates k_z as follows by the stratification:

$$j = 2hk_zN_0N^{-1}, \tag{A.10}$$

where h is the vertical scale of the thermocline. Frequency ω is related to the horizontal wavenumber and vertical wavenumbers by the dispersion relationship

$$\omega^2(k_h^2 + m^2) = k_h^2N^2 + m^2f_0^2, \tag{A.11}$$

where $m(j) \approx \frac{\pi}{h}j$. Making the hydrostatic approximation (i.e., ignoring the k_h^2/m^2 above) results in

$$\omega^2 = (\frac{N_0h}{\pi j})^2k_h^2 + f_0^2. \tag{A.12}$$

From the dispersion relationship (A.10), we can have

$$\frac{d\omega}{dk_h} = (\frac{N_0h}{\pi j})^2\frac{k_h}{\omega}, \tag{A.13}$$

then we can write the GM spectrum as a function of the horizontal wavenumber:

$$E_{GM}(k_h, j) = E_{GM}(\omega, j)\frac{d\omega}{dk_h}. \tag{A.14}$$

Following (Rocha et al., 2016), we obtain $\hat{D}^{\phi}_{W}(k)$ and $\hat{D}^{\psi}_{W}(k)$ by summing on j and transform the two-dimensional spectra to one-dimensional spectrum. Finally, we have:

$$\hat{D}^{\phi}_{k_x} = \frac{1}{\pi}\int_{|k|}^{\infty}\sum_{j}^{j_{max}} \frac{E_{GM}(k_h, j)}{k_h^2 + k_h^4/m^2}\sqrt{k_h^2 - k_x}dk_h. \tag{A.15}$$

Similary,

$$\hat{D}^{\psi}_{k_x} = \frac{1}{\pi}\int_{|k|}^{\infty}\sum_{j}^{j_{max}} \frac{f_0^2}{\omega^2}\frac{E_{GM}(k_h, j)}{k_h^2 + k_h^4/m^2}\sqrt{k_h^2 - k_x}dk_h \tag{A.16}$$

Now, $f_0^2/\omega_*^2(k_x) \overset{approx.}{=} \hat{D}^{\psi}_{k_x}/\hat{D}^{\phi}_{k_x}$ are known. With this in hand, equations of 3.41 and 3.42 can be solved, and finally fully wave-vortex decomposition is achieved.

The ratio from observation roughly follows the GM curve between 10 and 100 km (Fig. A.1). At smaller scales, the diagnosed ratio is much larger than the GM value, but the effects of both the interpolation onto a regular grid and the cutoff at the Nyquist wavenumber is likely contaminate the estimate. If diagnosed ratio is the same as GM value, we may interpret this flow is internal wave. The wavenumber at which not following GM values is assumed as the other physical processes. It is still reasonable to give an approximation for D^{ψ}/D^{ϕ} from GM model because using this way we can obtain decomposed energy at least the internal waves along Line P.

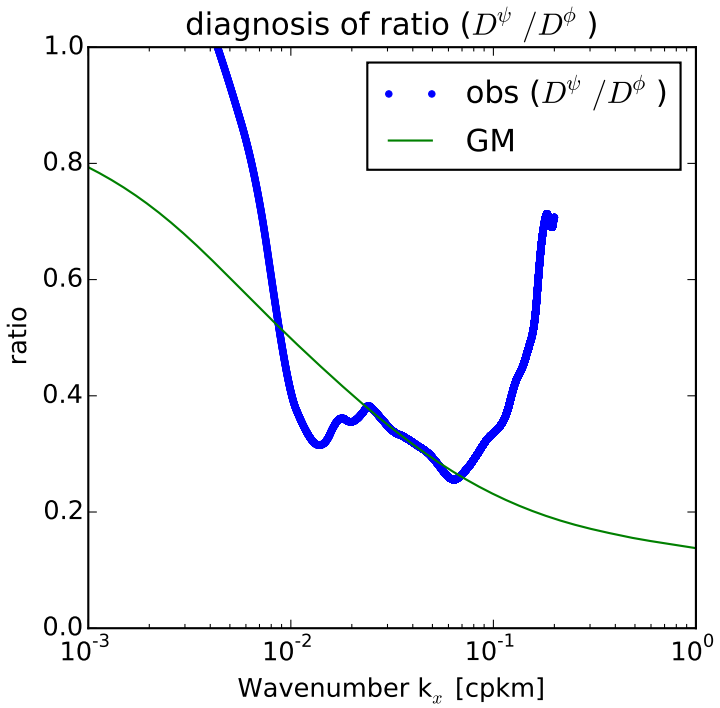

Figure A.1: Observations from the North Pacific: ratio D^{ψ}/D^{ϕ} compared to f^2/ω_*^2 from the Garrett Munk (GM) spectrum

A.3 Observed velocities

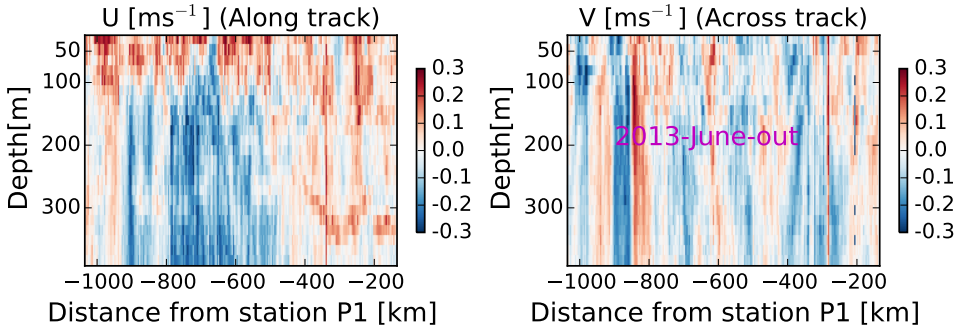

Figure A.2: Observational along-track and across-track velocity in June 2013 when the ship goes from station P1 to Station P26.

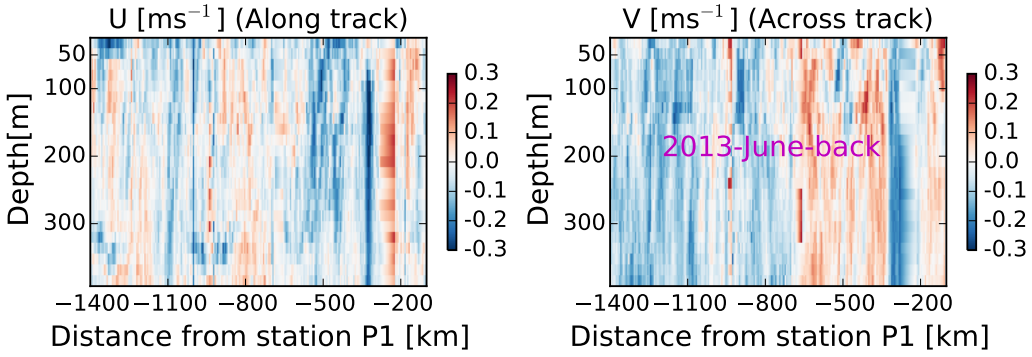

Figure A.3: Observational along-track and across-track velocity in June 2013 when the ship goes from Station P26 to station P1.

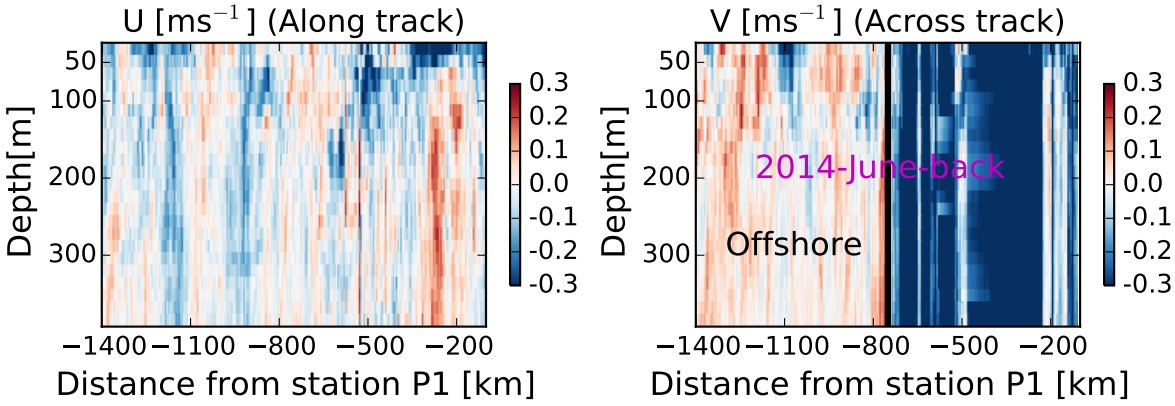

Figure A.4: Observational along-track and across-track velocity in June 2014 when the ship goes from Station P26 to station P1.

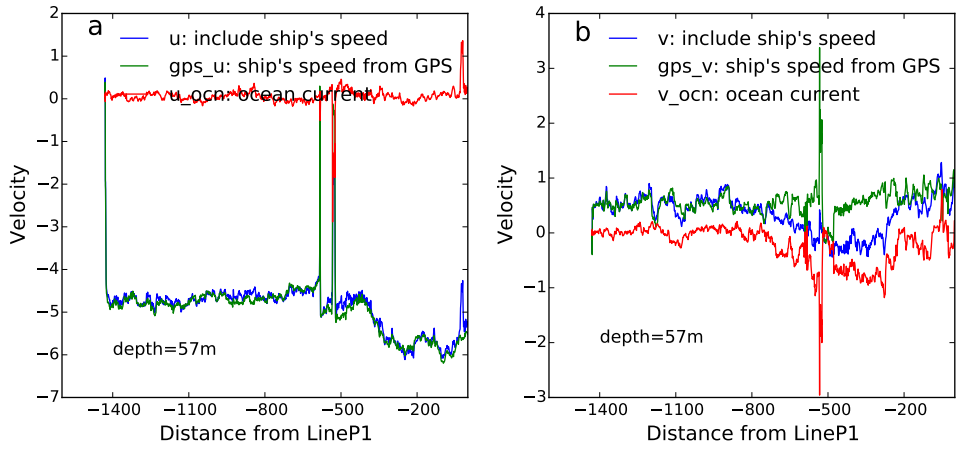

Figure A.5: Observed velocity at 57 m in directions of east-west (a) and north-south (b); blue lines show the observed total velocity include the ship's speed, green lines show the ship's speed from GPS, red lines represent ocean current velocity.

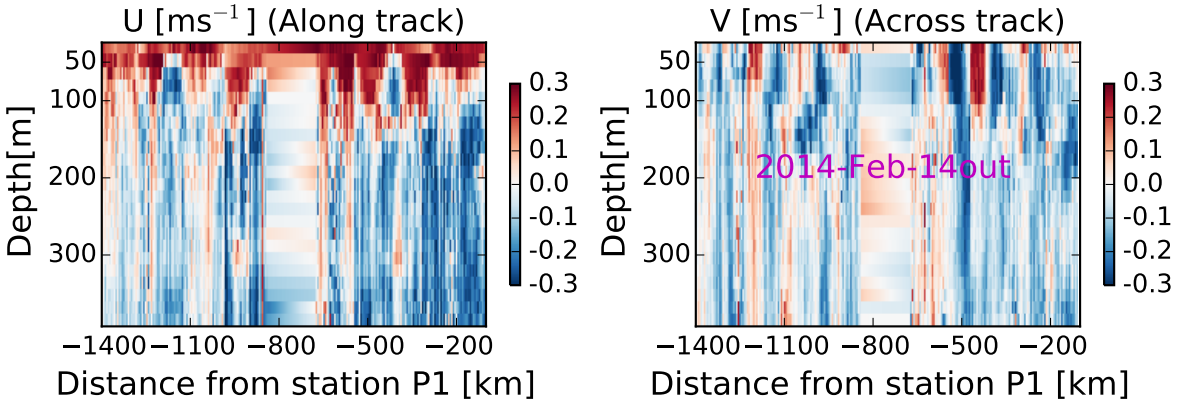

Figure A.6: Observational along-track and across-track velocity in February 2014 when the ship goes from station P1 to Station P26.

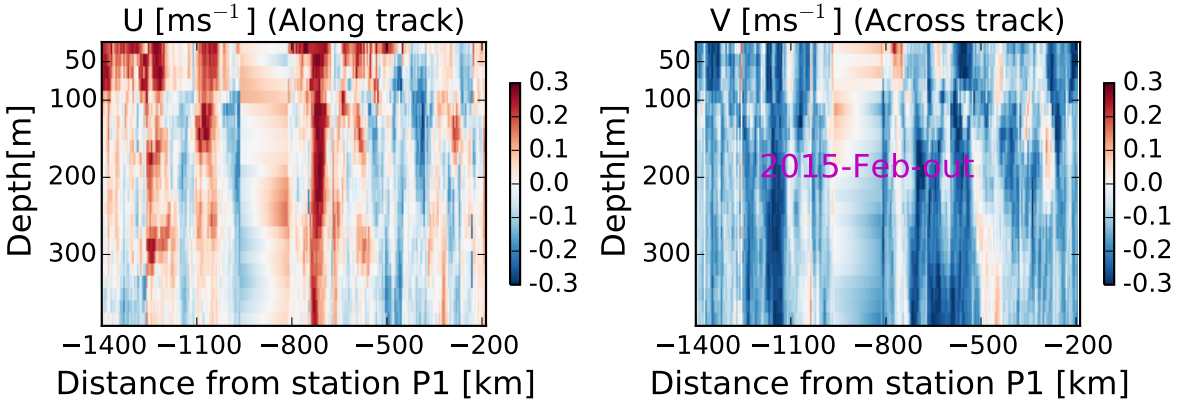

Figure A.7: Observational along-track and across-track velocity in February 2015 when the ship goes from station P1 to Station P26.

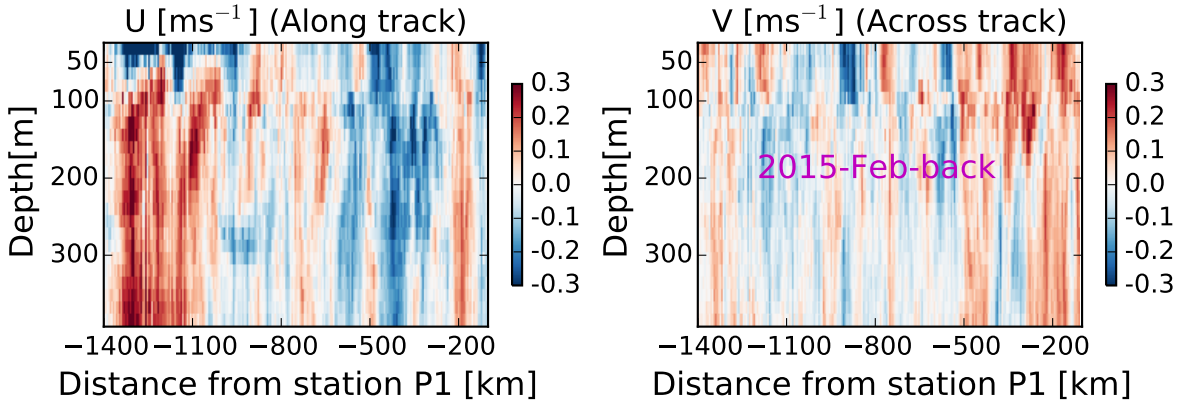

Figure A.8: Observational along-track and across-track velocity in February 2015 when the ship goes from Station P26 to station P1.

Bibliography

Jörn Callies and Raffaele Ferrari. Interpreting Energy and Tracer Spectra of Upper-Ocean Turbulence in the Submesoscale Range (1200 km). *Journal of Physical Oceanography*, 43:2456–2474, 2013. ISSN 0022-3670. doi: 10.1175/JPO-D-13-063.1. URL http://journals.ametsoc.org/doi/abs/10.1175/JPO-D-13-063.1.

P. Y. Le Traon, P. Klein, Bach Lien Hua, and G. Dibarboure. Do Altimeter Wavenumber Spectra Agree with the Interior or Surface Quasigeostrophic Theory? *Journal of Physical Oceanography*, 38(2001):1137–1142, 2008. ISSN 0022-3670. doi: 10.1175/2007JPO3806.1.

A Mahadevan. Eddy effects on biogeochemistry. *Nature*, 506:168–169, 2014.

M. Jeroen Molemaker, James C. Mcwilliams, Irad Yavneh, and Xavier Capet. Balanced and unbalanced routes to dissipation in an equilibrated Eady flow. *Journal of Physical Oceanography*, 654(9): 35–63, 2005. ISSN 0022-3670. doi: 10.1175/JPO2770.1. URL http://search.ebscohost.com/login.aspx?direct=true&profile=ehost&scope=site&auth

M. Jeroen Molemaker, James C. Mcwilliams, and Xavier Capet. Balanced and unbalanced routes to dissipation in an equilibrated Eady flow. *Journal of Fluid Mechanics*, 654:35–63, 2010. ISSN 0022-1120. doi: 10.1017/S0022112009993272.

X. Capet, J. C. McWilliams, M. J. Molemaker, and a. F. Shchepetkin. Mesoscale to Submesoscale Transition in the California Current System. Part III: Energy Balance and Flux. *Journal of Physical Oceanography*, 38(Charney 1971):29–43, 2008a. ISSN 0022-3670. doi: 10.1175/2007JPO3671.1. URL http://journals.ametsoc.org/doi/abs/10.1175/2007JPO3671.1.

G. Lapeyre and P. Klein. Dynamics of the Upper Oceanic Layers in Terms of Surface

Quasigeostrophy Theory. *Journal of Physical Oceanography*, 36:165–176, 2006. ISSN 0022-3670. doi: 10.1175/JPO2840.1.

Oliver Bühler, Jörn Callies, and Raffaele Ferrari. Wavevortex decomposition of one-dimensional ship-track data. *Journal of Fluid Mechanics*, 756: 1007–1026, 2014. ISSN 0022-1120. doi: 10.1017/jfm.2014.488. URL http://journals.cambridge.org/action/displayAbstract?aid=9346686 file:///Users/seb/Dropbox/Library.papers3/Files/56/5637C799-0069-4BC2-8CD4-0A7CC papers3://publication/doi/10.1017/jfm.2014.488.

Dong-Ping Wang, Charles N. Flagg, Kathleen Donohue, and H. Thomas Rossby. Wavenumber Spectrum in the Gulf Stream from Shipboard ADCP Observations and Comparison with Altimetry Measurements. *Journal of Physical Oceanography*, 40(2008):840–844, 2010. ISSN 0022-3670. doi: 10.1175/2009JPO4330.1.

Cesar B. Rocha, Teresa K. Chereskin, Sarah T. Gille, and Dimitris Menemenlis. Mesoscale to submesoscale wavenumber spectra in Drake Passage. *Journal of Physical Oceanography*, pages 1–17, 2016. ISSN 0022-3670. doi: 10.1175/JPO-D-15-0087.1.

William Crawford, Jake Galbraith, and Nick Bolingbroke. Line P ocean temperature and salinity, 1956-2005. *Progress in Oceanography*, 75(2):161–178, 2007. ISSN 00796611. doi: 10.1016/j.pocean.2007.08.017.

Jody M Klymak, William Crawford, Matthew H Alford, Jennifer a Mackinnon, and Robert Pinkel. Journal of Geophysical Research : Oceans. pages 2287–2307, 2015. doi: 10.1002/2013JC009421.Received.

Charney. Geostrophic Turbulence. *J. Atmos. Sci.*, 28(6):1087–1095, 1971.

William1978.

Detlef Stammer. Global Characteristics of Ocean Variability Estimated from Regional TOPEX/POSEIDON Altimeter Measurements. *Journal of Physical Oceanography*, 27(8):1743–1769, 1997. ISSN 0022-3670. doi: 10.1175/1520-0485(1997)027¡1743:GCOOVE¿2.0.CO;2.

R. K. Scott. Local and nonlocal advection of a passive scalar. *Physics of Fluids*, 18 (11), 2006. ISSN 10706631. doi: 10.1063/1.2375020.

J. H. LaCasce. Surface Quasigeostrophic Solutions and Baroclinic Modes with Exponential Stratification. *Journal of Physical Oceanography*, 42:569–580, 2012. ISSN 0022-3670. doi: 10.1175/JPO-D-11-0111.1.

X. Capet, J. C. McWilliams, M. J. Molemaker, and a. F. Shchepetkin. Mesoscale to Submesoscale Transition in the California Current System. Part I: Flow Structure, Eddy Flux, and Observational Tests. *Journal of Physical Oceanography*, 38(1): 29–43, 2008b. ISSN 0022-3670. doi: 10.1175/2007JPO3671.1.

B. J. Hoskins and F. P. Bretherton. Atmospheric Frontogenesis Models: Mathematical Formulation and Solution, 1972. ISSN 0022-4928.

Boyd. The Energy Spectrum of Fronts: Time Evolution of Shocks in Burger's Equation. *J. Atmos. Sci.*, 49(2):128–139, 1992.

G.K. Batchelor. *The theory of Homogeneous Turbulence*. Cambridge University Press, 1953.

C. E. Leith. Atmospheric Predictability and Two-Dimensional Turbulence, 1971. ISSN 0022-4928.

Li Zhai, Youyu Lu, Simon Higginson, Fraser Davidson, Fr??d??ric Dupont, Fran??ois Roy, J??r??me Chanut, and Gregory C. Smith. High-resolution modeling of the mean flow and meso-scale eddy variability around the Grand Banks of Newfoundland. *Ocean Dynamics*, 65(6):877–887, 2015. ISSN 16167228. doi: 10.1007/s10236-015-0839-5.

Gregory C. Smith, Francois Roy, Philip Mann, Frederic Dupont, Bruce Brasnett, Jean Francois Lemieux, Stephane Laroche, and Stephane Belair. A new atmospheric dataset for forcing ice-ocean models: Evaluation of reforecasts using the Canadian global deterministic prediction system. *Quarterly Journal of the Royal Meteorological Society*, 140(680):881–894, 2014. ISSN 1477870X. doi: 10.1002/qj.2194.

Patrice Klein, Bach Lien Hua, Guillaume Lapeyre, Xavier Capet, Sylvie Le Gentil, and Hideharu Sasaki. Upper Ocean Turbulence from High-Resolution 3D Simulations. *Journal of Physical Oceanography*, 38:1748–1763, 2008. ISSN 0022-3670. doi: 10.1175/2007JPO3773.1.

Sylvia T. Cole, Daniel L. Rudnick, and John a. Colosi. Seasonal evolution of upper-ocean horizontal structure and the remnant mixed layer. *Journal of Geophysical Research: Oceans*, 115:1–15, 2010. ISSN 21699291. doi: 10.1029/2009JC005654.

Sylvia T. Cole and Daniel L. Rudnick. The spatial distribution and annual cycle of upper ocean thermohaline structure. *Journal of Geophysical Research*, 117 (C2):C02027, feb 2012. ISSN 0148-0227. doi: 10.1029/2011JC007033. URL `http://doi.wiley.com/10.1029/2011JC007033`.

Raffaele Ferrari and Daniel L. Rudnick. Thermohaline variability in the upper ocean. *Journal of Geophysical Research*, 105(C7):16857, 2000. ISSN 0148-0227. doi: 10.1029/2000JC900057. URL `http://doi.wiley.com/10.1029/2000JC900057`.